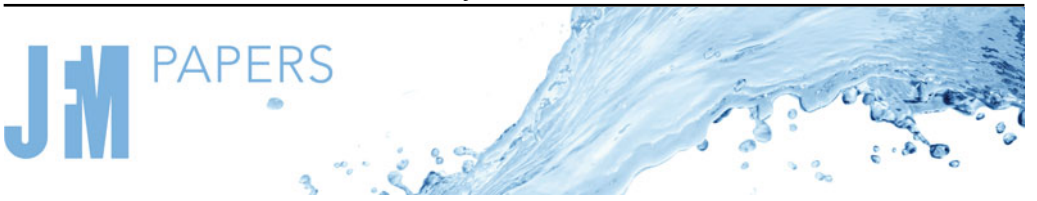
J. Fluid Mech. (2025), *vol.* 1011, A22, doi:10.1017/jfm.2025.398



Pseudo-turbulence induced by settling spheroids in a quiescent fluid

Xinyu Jiang[1], **Luca Brandt**[2,3,4], **Chunxiao Xu**[1] **and Lihao Zhao**[1,5]

[1]AML, Department of Engineering Mechanics, Tsinghua University, 100084 Beijing, PR China

[2]Department of Environmental, Land and Infrastructure Engineering (DIATI), Politecnico di Torino, 10129 Turin, Italy

[3]FLOW, Department of Engineering Mechanics, KTH Royal Institute of Technology, Stockholm, Sweden

[4]Department of Energy and Process Engineering, Norwegian University of Science and Technology (NTNU), Trondheim, Norway

[5]State Key Laboratory of Advanced Space Propulsion, Tsinghua University, 100084 Beijing, PR China

Corresponding author: Lihao Zhao, zhaolihao@tsinghua.edu.cn

(Received 12 November 2024; revised 1 March 2025; accepted 11 April 2025)

In this study, we investigate the sedimentation of spheroidal particles in an initially quiescent fluid by means of particle-resolved direct numerical simulations. Settling particles with three different shapes – oblate spheroid, sphere and prolate spheroid – but fixed Galileo number $Ga = 80$ and density ratio $\gamma = 2$ at volume fraction $\phi = 1\%$ are considered. Oblate and prolate particles are found to form column-like clusters as a consequence of the wake-induced hydrodynamic interactions in the suspension. This effect, together with the change of particle orientation, enhances the mean settling velocity of the dispersed phase. In contrast, spherical particles do not exhibit clustering, and settle with hindered velocity in the suspension. Furthermore, we focus on the pseudo-turbulence induced by the settling particles. We report a non-Gaussian distribution of the fluid velocity and a robust -3 power law of the energy spectra. By scrutinizing the scale-by-scale budget, we find that the anisotropy of the particle-induced pseudo-turbulence is manifested not only by the uneven allocation of turbulence kinetic energy among the different velocity components, but also by the anisotropic distribution of energy in spectral space. The fluid–particle interactions inject energy into the vertical velocity component, thus sustaining the turbulence, while pressure redistributes the kinetic energy among the different velocity components. The clustering of oblate/prolate particles significantly increases the energy input at large scales, forcing elongated flow structures. Moreover, the redistribution and nonlinear transfer of the energy are also intensified in the presence of particle clustering, which reduces the anisotropy of the particle-induced pseudo-turbulence.

Key words: particle/fluid flows, homogeneous turbulence

© The Author(s), 2025. Published by Cambridge University Press.

https://doi.org/10.1017/jfm.2025.398 Published online by Cambridge University Press

1. Introduction

The gravity-driven settling of particles is widely encountered in environmental and industrial applications (Guazzelli & Hinch 2011; Brandt & Coletti 2022). Examples include precipitations in the atmosphere (Pruppacher & Klett 2010), the marine snow of settling plankton or debris (Trudnowska *et al.* 2021), the deposition of ashes after a volcanic eruption (Rossi *et al.* 2021), and reacting particles in fluidized beds (Zhou *et al.* 2011). Despite the relatively simple configurations often investigated, the problem is inherently complex and determined by several parameters, such as particle size, density and shape, as well as the fluid and flow characteristics. From a fundamental viewpoint, the settling rate and dynamics of the particle phase, and the particle-induced modulation of the underlying flows, which involve complicated interactions between a large number of settling particles and the carrier fluid flows, are highly relevant in the aforementioned applications and have therefore been the object of several studies (Batchelor 1972; Caflisch & Luke 1985; Guazzelli & Hinch 2011; Brandt & Coletti 2022).

Concerning the settling motion of multiple spheres in suspensions, many studies have been performed in the past decades. Among these, we recall the pioneering work by Richardson & Zaki (1954), who proposed the well-known idea of hindered settling of particles in the Stokes flow regime. Specifically, the upward mean flow, arising to compensate the particle downward motion, increases the total drag forces experienced by particles, so as to reduce their mean settling speed (Di Felice 1999). As no analytical expression can be found even for monodisperse spheres, many efforts have been made to improve the empirical correlation of the hindered settling velocity as a function of the particle volume fraction and settling Reynolds number (Garside & Al-Dibouni 1977; Di Felice 1999; Yin & Koch 2007). Moreover, when the particle and fluid inertia become relevant, an enhancement of the particle settling speed in suspensions was initially reported by Kajishima & Takiguchi (2002) and Kajishima (2004). Since then, with the help of particle-resolved direct numerical simulation (PR-DNS), the enhanced settling rate of particles has been related to the formation of column-like clusters in dilute suspensions provided that the settling Reynolds number is high enough (approximately greater than 175) (Uhlmann & Doychev 2014; Zaidi *et al.* 2014; Zaidi 2018; Shajahan & Breugem 2023). These findings were also confirmed by the experiments conducted by Huisman *et al.* (2016).

The formation of particle clusters is attributed to the hydrodynamic interactions among settling spheres (Zaidi *et al.* 2014). In particular, we recall the drafting–kissing–tumbling (DKT) interactions (Fortes *et al.* 1987) between a pair of initially vertically aligned settling spheres. In this configuration, the rear particle, located in the wake of the leading one, experiences downward flows and thus accelerates its settling motion, which results in an attraction of the two spheres (drafting stage). Then the two particles touch and form an elongated body aligning vertically (kissing stage). Finally, as the elongated configuration is unstable, the two particles tumble under the effect of fluid inertia, and separate rapidly afterwards (tumbling stage). Similarly, in a suspension with multiple settling particles, the attraction and entrapment of particles in the wakes of upstream particles give rise to the formation of particle clusters with column-like arrangements (Uhlmann & Doychev 2014; Zaidi *et al.* 2014). As the consequence of the settling velocity of particle clusters being greater than that of the isolated particle, the mean settling rate of particles in the suspension can be enhanced substantially.

In the practical applications, particles are often non-spherical in shape, so they are commonly modelled as spheroids in earlier studies (Voth & Soldati 2017). Compared to the well-studied cases of settling spherical particles, less is known about the settling of non-spherical particles, especially in the finite-fluid-inertia regime. In Fornari *et al.* (2018), the

https://doi.org/10.1017/jfm.2025.398 Published online by Cambridge University Press

settling of oblate particles with aspect ratio (the ratio between the polar and equator axes) $1/3$ and different volume fractions was investigated numerically. It was demonstrated that oblate particles can form notable clusters even at a relative low settling Reynolds number (approximately 40), leading to a significant enhancement of the mean settling velocity. The difference compared to the cases of settling spheres is ascribed to the stable piled-up structures of a pair of settling oblate spheroids undergoing DKT interactions (Ardekani *et al.* 2016). Similarly, Moriche *et al.* (2023) considered particles with a lower non-sphericity, aspect ratio $2/3$, and reported that the easier attraction between settling oblate spheroids induces large-scale particle clusters with a long extension along the vertical direction. More recently, we studied the settling of prolate particles with aspect ratio 3 over a wide range of volume fractions from 0.1 % to 10 %, and found a non-monotonic variation of the particle settling velocity as the volume fraction increases (Jiang *et al.* 2024*b*). This phenomenon was explained by the combined effects of particle clustering, changes in orientation and the fluid hindrance on the settling motion of particle swarms.

From another point of view, the fluid flow induced by the gravity-driven motion of a dispersed phase is also a hot spot in the community of multiphase flow research. For example, the bubble-induced agitation generates a complex spatiotemporal flow, so-called pseudo-turbulence (Risso 2018), which has been widely studied by experiments (Lance & Bataille 1991; Riboux *et al.* 2010; Roghair *et al.* 2011) and numerical simulations (Innocenti *et al.* 2021; Hidman *et al.* 2023; Pandey *et al.* 2020, 2023). Unlike canonical turbulence where the energy is injected into the system by the large-scale flow shear, the pseudo-turbulence gains energy from the dispersed bubbles (Risso 2018) with three features. First, it is anisotropic with larger fluctuations of vertical velocity than those of the horizontal component (Riboux *et al.* 2010; Amoura *et al.* 2017). Second, the probability density function (p.d.f.) of the velocity fluctuation is non-Gaussian, with a skewed distribution of the vertical velocity fluctuations and exponential tails for the p.d.f. of the horizontal velocity fluctuations (Martínez-Mercado *et al.* 2007; Riboux *et al.* 2010). Third, the energy spectra is characterized by a κ^{-3} (where κ is the wavenumber) power-law scaling on the scale comparable to or smaller than the bubble size (Lance & Bataille 1991; Martínez-Mercado *et al.* 2007; Roghair *et al.* 2011; Innocenti *et al.* 2021), rather than the classical $\kappa^{-5/3}$ power law of the single-phase turbulence. In Lance & Bataille (1991), the κ^{-3} power law of the energy spectra was explained by the assumption of local balance between the energy production and dissipation in the wake of the rising bubbles. Recently, Pandey *et al.* (2023) reported the co-existence of Kolmogorov turbulence (the $\kappa^{-5/3}$ power law) and pseudo-turbulence in the bubble-induced turbulence (the κ^{-3} power law), provided that the Reynolds number of the rising bubbles is sufficiently high.

However, the pseudo-turbulence induced by the interactions between heavy particles and a carrier fluid has received less attention so far. Mehrabadi *et al.* (2015) numerically investigated the fluid flows past fixed or freely moving particle assemblies. They found that the degree of anisotropy in the Reynolds stresses depends on the volume fraction and the Reynolds number based on the mean slip velocity, and the mobility of the dispersed particles can influence the intensity of the pseudo-turbulence. Using point-particle DNS, Capecelatro *et al.* (2014, 2015) investigated the gravity-driven motion of particles in an initially still fluid. The two-way coupling between the two phases leads to the local accumulation of settling particles (with particle Reynolds number $Re_p \sim O(1)$), which in turn generates and sustains turbulence in the fluid phase. Concerning the finite-size particles, the fluid flow induced by settling particles was also studied primarily in the initially turbulent or quiescent environment (Fornari *et al.* 2018, 2019). It was reported that the particle-induced turbulence is anisotropic with unequal velocity fluctuations for different velocity components.

https://doi.org/10.1017/jfm.2025.398 Published online by Cambridge University Press

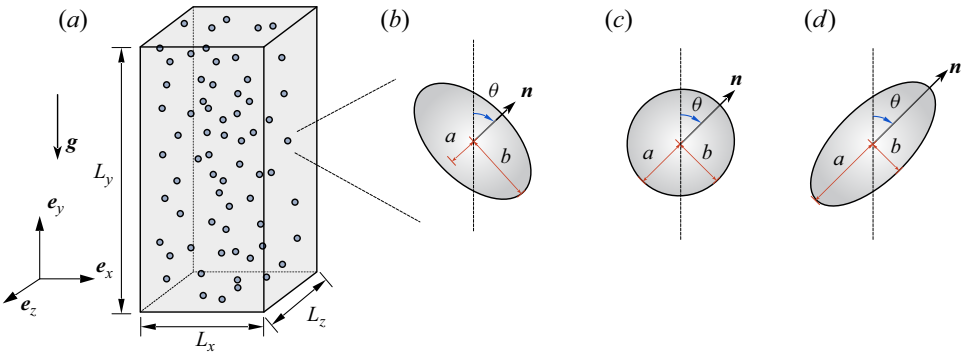


Figure 1. (*a*) Schematic representation of the sedimentation of spheroidal particles in a quiescent fluid. Three different shapes of particle are considered: (*b*) oblate particles with aspect ratio $\lambda = 0.5$; (*c*) spherical particles with $\lambda = 1$; and (*d*) prolate particles with $\lambda = 2$. The angle θ represents the angle between the vertical direction and the symmetry axis of the spheroid (denoted by $\boldsymbol{n}$).

Inspired by the above literature review, we aim to investigate the characteristics of pseudo-turbulence in suspensions of settling particles. In particular, we are interested in how the presence of particle clustering influences the features of the particle-induced pseudo-turbulence. To this end, we perform PR-DNS of settling particles with three different shapes, i.e. oblate spheroids, spheres and prolate spheroids. We find that non-spherical particles, especially settling oblate spheroids, are prone to form column-like clusters in the suspension. As for the fluid phase, we identify a robust κ^{-3} power-law scaling in the energy spectrum of the particle-induced turbulent flows. Moreover, we find that the energy transfer in this kind of fluid flow is significantly affected by the particle clustering, which is found to enhance the energy input at large scales, facilitate the nonlinear transfer among scales, and promote energy redistribution to reduce the anisotropy of the pseudo-turbulence.

The remainder of this paper is organized as follows. In § 2, we introduce the flow configuration of this study, describe the numerical method of the PR-DNS based on the immersed boundary method, and introduce the observables in this study. In § 3, we focus on the collective behaviour of the dispersed phase, discussing the shape effect on the settling velocity and clustering of the particles. We concentrate on the turbulent flow induced by the settling particles in § 4, reporting the basic statistics of the fluid velocity fluctuations, and investigating the energy spectra and the budget of the turbulence kinetic energy. Finally, we summarize the key findings and draw conclusions in § 5.

2. Methodology

2.1. *Flow configuration and parameter setting*

In the present work, we numerically study the sedimentation of spheroidal particles in a triply periodic domain filled with initially quiescent fluid (figure 1*a*). The shape of the spheroidal particles is described by the aspect ratio $\lambda = a/b$, where a and b denote the polar and equatorial radii of the spheroid, as shown in figure 1(*b–d*). The solid volume fraction, defined by $\phi = (\pi/6)(N_p D_{eq}^3)/(L_x L_y L_z)$, is set to $\phi = 1\,\%$. This corresponds to $N_p = 3129$ particles in a computational domain with size $L_x \times L_y \times L_z = 32D_{eq} \times 160D_{eq} \times 32D_{eq}$, where D_{eq} is the equivalent diameter of the particle (the diameter of a sphere with the same volume as the spheroid). The gravity is applied in the negative y direction, and the ratio between the gravitational force and the viscous force is measured

https://doi.org/10.1017/jfm.2025.398 Published online by Cambridge University Press

Case	Particle motion	Particle shape	Re_{s0}	θ_0	T_{stat}/v_{s0}
1	FM	Oblate ($\lambda = 0.5$)	63.3	0°/180°	200
2	FM	Spherical ($\lambda = 1$)	80.9	Arbitrary	150
3	FM	Prolate ($\lambda = 2$)	69.4	90°	200
4	FRP	Oblate ($\lambda = 0.5$)	63.3	0°/180°	20
5	FRP	Spherical ($\lambda = 1$)	80.9	Arbitrary	20
6	FRP	Prolate ($\lambda = 2$)	69.4	90°	20

Table 1. Set-ups for the simulation cases considered in the present study. The cases with freely moving particles are denoted by 'FM', while 'FRP' represents particles with fixed relative positions. The settling Reynolds number and the pitch angle for the isolated settling spheroid are denoted by Re_{s0} and θ_0, respectively.

by the Galileo number $Ga = \sqrt{(\gamma - 1)\,\|\boldsymbol{g}\|\,D_{eq}^3}/\nu$. Here, $\gamma = \rho_p/\rho_f$ is the density ratio between particle and fluid, $\boldsymbol{g}$ is the gravitational acceleration, and ν is the kinematic viscosity of the fluid. In the present study, we set the Galileo number as $Ga = 80$, and consider settling particles with different shapes. The choice of this dimensionless parameter is motivated by the different DKT interactions for pairwise settling spheroids with different shapes at $Ga = 80$ (Ardekani *et al.* 2016). The particle–fluid density ratio is set as $\gamma = 2$, which is a typical value for the solid–liquid scenario (Seyed-Ahmadi & Wachs 2021). In total, we consider six simulation cases with three kinds of spheroidal particles: oblate particles with $\lambda = 0.5$, spherical particles with $\lambda = 1$, and prolate particles with $\lambda = 2$, as listed in table 1. With these parameter set-ups, we observe a significant clustering for freely moving oblate and prolate particles in the suspension (see the discussion in § 3.3). We note that the full decorrelation of the vertical fluid velocity is not attained when particle clustering occurs. Similar finite correlations were also reported in previous studies on settling particles (Uhlmann & Doychev 2014; Moriche *et al.* 2023), and are difficult to eliminate by only increasing the size of the computational domain. Considering the limited influence of the domain size on the behaviour of settling particles (Zaidi 2021) and the computational cost, we do not further enlarge the domain size in the current simulations. Additionally, as the reference cases, we simulate the settling of an isolated spheroid before conducting the simulations of multiple particles, and obtain the settling Reynolds number $Re_{s0} = v_{s0}D_{eq}/\nu$ for each type of particle (see table 1). Owing to the relatively low Reynolds number for the particle settling motion under the present parameter set-up, the rear wake of the isolated settling particle remains stable, so the path instability is not triggered (Jenny *et al.* 2004; Ern *et al.* 2012). Additionally, we find in the simulation that the isolated settling oblate/prolate spheroid reorients with the major axis perpendicular to the gravitational direction, although a random inclined orientation is prescribed as the initial condition, due to the effect of fluid inertial torque (Ardekani *et al.* 2016). Moreover, we also perform simulations of settling particles with fixed relative positions and frozen orientations; see table 1. The objective of these artificial simulations is to clarify the effect of particle clustering on the particle-induced turbulence, which is elaborated in § 4.

In each simulation, particles are initially seeded with random orientations and random positions in the computational domain, without overlaps. Readers can refer to Anoukou *et al.* (2018) for the generation of initial particle assemblies. The statistics given in §§ 3 and 4 are obtained after the system has reached a fully developed state, which is ensured by monitoring the time evolution of the particle-averaged settling velocity in the simulation. The duration of the time window over which we compute the statistics, denoted by T_{stat}, is provided in table 1. This time interval is extended for the cases with freely moving particles to allow for the organization of particle micro-structures in these cases.

https://doi.org/10.1017/jfm.2025.398 Published online by Cambridge University Press

2.2. *Fluid solver and immersed boundary method*

The fluid flow is governed by the incompressible Navier–Stokes equations:

$$\nabla \cdot \boldsymbol{u} = 0, \tag{2.1}$$

$$\frac{\partial \boldsymbol{u}}{\partial t} + \boldsymbol{u} \cdot \nabla \boldsymbol{u} = -\nabla p + \frac{1}{Re}\nabla^2 \boldsymbol{u} + \boldsymbol{f}. \tag{2.2}$$

Here, $\boldsymbol{u} = (u, v, w)$ denotes the velocity of the fluid flow, p is the pressure, and $\boldsymbol{f}$ is the immersed boundary (IB) forcing term (IB force). Note that (2.1)–(2.2) are presented in dimensionless form, and the Reynolds number $Re = U_0 L_0/\nu$ is defined based on the characteristic velocity (U_0) and length (L_0) of the fluid flow. Here, we set the settling velocity of an isolated particle as the characteristic velocity and the equivalent diameter as the character length, i.e. $U_0 = v_{s0}$ and $L_0 = D_{eq}$. The IB forces in (2.2) are employed to resolve the interactions between the rigid particles and the fluid flows (as elaborated in the following).

To solve (2.1)–(2.2) numerically, we adopt a fractional step method for the decoupling of velocity and pressure (Kim *et al.* 2002). Using the Crank–Nicolson scheme for the temporal discretization of the convection and viscous terms, the temporal advancement of (2.1)–(2.2) from the nth to the $(n+1)$th time step is written as (Kim *et al.* 2002)

$$\frac{\boldsymbol{u}^* - \boldsymbol{u}^n}{\Delta t} + \frac{1}{2}(H(\boldsymbol{u}^*) + H(\boldsymbol{u}^n)) = -Gp^{n-1/2} + \frac{1}{2\,Re}\left(L\boldsymbol{u}^* + L\boldsymbol{u}^n\right), \tag{2.3}$$

$$\boldsymbol{u}^{**} = \boldsymbol{u}^* + \Delta t\, \boldsymbol{f}^{n+1/2}, \tag{2.4}$$

$$DG\,\delta p = D\boldsymbol{u}^{**}/\Delta t, \tag{2.5}$$

$$p^{n+1/2} = p^{n-1/2} + \delta p, \tag{2.6}$$

$$\boldsymbol{u}^{n+1} = \boldsymbol{u}^{**} - \Delta t\, G\, \delta p. \tag{2.7}$$

Here, H, G, L and D represent the spatial discrete convection, gradient, Laplacian and divergence operators, which are evaluated by the central finite-difference scheme on a staggered Eulerian grid (Kim *et al.* 2002). The first prediction velocity $\boldsymbol{u}^*$ is updated without considering the IB forces in (2.3). The second prediction velocity $\boldsymbol{u}^{**}$ is then computed by (2.4) with the introduction of IB forces. Finally, the velocity projection step is performed by solving the Poisson equation (2.5), updating the pressure as in (2.6), and updating the velocity by (2.7).

To impose the no-slip boundary condition on the particle surfaces, we employ the direct-forcing IB method to calculate the IB forces (Uhlmann 2005; Breugem 2012):

$$\boldsymbol{U}_l^* = \sum_{ijk} \boldsymbol{u}_{ijk}^*\, \delta\left(\boldsymbol{X}_l^n - \boldsymbol{x}_{ijk}\right)\, \Delta h^3, \tag{2.8}$$

$$\boldsymbol{F}_l^{n+1/2} = \frac{\boldsymbol{U}_p(\boldsymbol{X}_l^n) - \boldsymbol{U}_l^*}{\Delta t}, \tag{2.9}$$

$$\boldsymbol{f}_{ijk}^{n+1/2} = \sum_l \boldsymbol{F}_l^{n+1/2}\, \delta\left(\boldsymbol{x}_{ijk} - \boldsymbol{X}_l^n\right) \Delta V_l. \tag{2.10}$$

Here, the capital letters refer to variables defined on the Lagrangian marker points allocated on the particle surface. In (2.8), the first prediction velocity $\boldsymbol{u}^*$ is interpolated from the Eulerian grid points to the Lagrangian marker points using the Dirac delta function $\delta(\cdot)$, where $\boldsymbol{X}_l^n$ denotes the position of the lth Lagrangian marker point. Then the IB force is obtained on the Lagrangian marker point from (2.9), with $\boldsymbol{U}_p$ representing the rigid-body velocity of the particle. Finally, the IB forces are spread onto the Eulerian

https://doi.org/10.1017/jfm.2025.398 Published online by Cambridge University Press

grid with the Dirac delta function via (2.10), in which ΔV_l denotes the volume associated with the lth Lagrangian marker point. The Dirac delta function presented in (2.8) and (2.10) is defined by

$$\delta(\boldsymbol{x}) = \frac{1}{\Delta h^3} \times \phi\left(\frac{x}{\Delta h}\right) \times \phi\left(\frac{y}{\Delta h}\right) \times \phi\left(\frac{z}{\Delta h}\right), \tag{2.11}$$

in which $\phi(\cdot)$ is a 3-grid-width discrete Dirac delta function (Roma *et al.* 1999):

$$\phi(r) = \begin{cases} \dfrac{1}{6}(5 - 3|r| - \sqrt{-3(1-|r|)^2 + 1}), & 0.5 \leqslant |r| \leqslant 1.5, \\ \dfrac{1}{3}(1 + \sqrt{-3r^2 + 1}), & |r| \leqslant 0.5, \\ 0, & \text{otherwise}. \end{cases} \tag{2.12}$$

In the present study, a uniform Eulerian grid with an equal spacing in the three directions, i.e. $\Delta h = \Delta x = \Delta y = \Delta z = D_{eq}/24$, is utilized. This grid size has been validated to be fine enough to resolve the particle–fluid interaction in the simulation of the isolated settling particle. The time step for the simulation is set as $\Delta t = 0.01 D_{eq}/v_{s0}$ for each case, leading to the Courant number (based on the isolated settling velocity) $CFL = 0.24$. Furthermore, for the implementation of the direct-forcing IB method, we employ the multi-forcing scheme with $N_s = 2$ iterations, and consider the inward retraction of Lagrangian marker points with distance $r_d = 0.3\,\Delta h$ to better approximate the no-slip boundary condition on the particle surface (for more details, see Breugem 2012). Additionally, a zero flux constraint is imposed in the simulation by subtracting the spatially averaged IB forces after (2.10) at each time step (Chouippe & Uhlmann 2015; Höfler & Schwarzer 2000):

$$\boldsymbol{f}_{ijk}^{n+1/2} = \boldsymbol{f}_{ijk}^{n+1/2} - \langle \boldsymbol{f}_{ijk}^{n+1/2} \rangle_V, \tag{2.13}$$

where the operator $\langle \cdot \rangle_V$ represents the spatial average over the whole computational domain.

2.3. *Particle motion*

The motion of spheroidal particles in fluid flow is governed by the Newton–Euler equations:

$$\rho_p V_p \frac{\mathrm{d}\boldsymbol{v}}{\mathrm{d}t} = \boldsymbol{F}_H + \left(\rho_p - \rho_f\right) \boldsymbol{g} V_p + \boldsymbol{F}_C, \tag{2.14}$$

$$\frac{\mathrm{d}(\boldsymbol{I} \cdot \boldsymbol{\omega})}{\mathrm{d}t} = \boldsymbol{T}_H + \boldsymbol{T}_C, \tag{2.15}$$

where V_p denotes the particle volume, $\boldsymbol{I}$ is the moment of inertia of the particle, and $\boldsymbol{v} = (v_x, v_y, v_z)$ and $\boldsymbol{\omega}$ represent the particle translational and angular velocities. In the framework of the direct-forcing IB method, the force and torque exerted from fluid flow onto the particle, denoted by $\boldsymbol{F}_H$ and $\boldsymbol{T}_H$, can be computed by (Breugem 2012)

$$\boldsymbol{F}_H = -\rho_f \sum_l \boldsymbol{F}_l\, \Delta V_l + \rho_f \frac{\mathrm{d}}{\mathrm{d}t} \int_{V_p} \boldsymbol{u}\, \mathrm{d}V, \tag{2.16}$$

$$\boldsymbol{T}_H = -\rho_f \sum_l \boldsymbol{r} \times \boldsymbol{F}_l\, \Delta V_l + \rho_f \frac{\mathrm{d}}{\mathrm{d}t} \int_{V_p} \boldsymbol{r} \times \boldsymbol{u}\, \mathrm{d}V. \tag{2.17}$$

Refer to our previous works (Jiang *et al.* 2024*a*,*b*) for more details and validations of the aforementioned numerical method to simulate the particle–fluid interactions.

https://doi.org/10.1017/jfm.2025.398 Published online by Cambridge University Press

Moreover, the contact force ($\boldsymbol{F}_C$) and torque ($\boldsymbol{T}_C$) are included to account for the particle–particle collisions. In detail, we consider the lubrication force based on the model of Jeffrey (1982) when the surface-to-surface distance between two particles is smaller than one grid spacing, and apply the normal and tangential collision force based on the soft-sphere model for the touching particles (Costa *et al.* 2015). More details about the implementation and validation of the contact force can be found in Costa *et al.* (2015) and Ardekani *et al.* (2016).

Note that in the simulations of settling particles with fixed relative positions, we calculate the average of the hydrodynamic forces over all particles, i.e. (the subscript i refers to the particle counting)

$$\boldsymbol{F}_{H,avg} = \frac{1}{N_p}\sum_{i=1}^{N_p} \boldsymbol{F}_{H,i}, \tag{2.18}$$

and use $\boldsymbol{F}_{H,avg}$ to update the velocity of each particle in (2.14). In this manner, the particle velocities are identical so as to keep their initial relative positions without imposing a predefined settling speed. As regards the particle angular dynamics, (2.15) is not solved, so the orientation of the dispersed particles is frozen.

2.4. *Data analysis*

Here, we introduce the post-processing tools adopted in the present work. In particular, we use Voronoi analysis to examine particle clustering, and perform scale-by-scale budget analysis of the turbulent flow induced by the settling particles.

2.4.1. *Voronoi analysis*

In the present work, we examine the spatial distribution of dispersed particles by virtue of the Voronoi diagram (Monchaux *et al.* 2010). To quantify the clustering tendency, we define a dimensionless parameter, i.e. the clustering indicator C, as (Tagawa *et al.* 2013)

$$C = \sigma(\overline{V}_{Voro})/\sigma(\overline{V}_{Voro,rand}). \tag{2.19}$$

In the above definition, $\sigma(\overline{V}_{Voro})$ denotes the standard deviation of the normalized Voronoi volumes, and $V_{Voro,rand}$ represents the volume of tesselation for a random particle distribution. The normalized Voronoi volume of the ith particle is defined by

$$\overline{V}_{Voro}(i) = \frac{V_{Voro}(i)}{V_{tot}/N_p}, \tag{2.20}$$

in which $V_{tot} = L_x L_y L_z$ denotes the volume of the entire computational domain. According to the definition in (2.19), $C < 1$ indicates that the particle spatial distribution is closer to an orderly lattice-like arrangement than a random distribution. Conversely, if $C > 1$, then the system has a high tendency to clustering, with an increased number of regions with locally accumulated particles (clusters) and of empty regions (voids). Note that, unlike the case of point-particles (Ferenc & Néda 2007), the p.d.f. of the Voronoi volumes for a random distribution of finite-size particles does not conform to a Poisson distribution (Uhlmann 2020). Thus to compute the clustering indicator C by (2.19), we statistically obtain $\sigma(\overline{V}_{voro,rand})$ by repeatedly generating non-overlapping finite-sized particles with random positions (and also random orientations for non-spherical particles) (Anoukou *et al.* 2018).

https://doi.org/10.1017/jfm.2025.398 Published online by Cambridge University Press

2.4.2. *Particle-induced turbulence: scale-by-scale budget*

One objective of the present study is to understand the characteristics and energy transfer of the pseudo-turbulent flow (adopting the term used for the bubble-induced turbulence) induced by the settling particles. To this end, we will investigate the scale-by-scale energy budget of the particle-induced turbulent flow. Here, we briefly introduce the derivation of the fluid-phase energy budget equation in spectral space (see, among others, Crialesi-Esposito *et al.* 2022). First, we take the Fourier transform of the ith ($i = 1, 2, 3$) component of the momentum equation (2.2):

$$\frac{\partial \widetilde{u_i}}{\partial t} + \widetilde{G_i} = -\widetilde{P_i} + \widetilde{V_i} + \widetilde{f_i}. \tag{2.21}$$

Here, $G_i = u_j\,\partial u_i/\partial x_j$, $P_i = (1/\rho_f)\,\partial p/\partial x_i$ and $V_i = \partial^2 u_i/(\partial x_j\,\partial x_j)$ denote the nonlinear, pressure gradient and viscous terms, respectively. The notation $\tilde{g}(\boldsymbol{\kappa}, t)$ represents the Fourier mode at the wavenumber vector $\boldsymbol{\kappa} = (\kappa_x, \kappa_y, \kappa_z)$ of an arbitrary variable $g(\boldsymbol{x}, t)$ (g could be u_i, G_i, P_i, V_i or f_i) in the physical domain. Next, we multiply (2.21) with the complex conjugate of the velocity $\widetilde{u_i}^*$, leading to (no summation over index i)

$$\widetilde{u_i}^*\frac{\partial \widetilde{u_i}}{\partial t} + \widetilde{u_i}^*\widetilde{G_i} = -\widetilde{u_i}^*\widetilde{P_i} + \widetilde{u_i}^*\widetilde{V_i} + \widetilde{f_i}\widetilde{u_i}^*. \tag{2.22}$$

Taking the summation of (2.22) with its complex conjugate, we finally obtain the scale-by-scale budget equation for the ith velocity component:

$$\frac{\partial \mathcal{E}_i\,(\boldsymbol{\kappa}, t)}{\partial t} = \mathcal{T}_i\,(\boldsymbol{\kappa}, t) + \mathcal{P}_i\,(\boldsymbol{\kappa}, t) + \mathcal{D}_i\,(\boldsymbol{\kappa}, t) + \mathcal{F}_i\,(\boldsymbol{\kappa}, t)\,. \tag{2.23}$$

The physical interpretation of each term in (2.23) is as follows (without the use of Einstein's summation convention here):

(i) $\mathcal{E}_i(\boldsymbol{\kappa}, t) = (1/2)\widetilde{u_i}\widetilde{u_i}^*$ is the energy of the velocity component u_i in the spectral domain
(ii) $\mathcal{T}_i(\boldsymbol{\kappa}, t) = -(1/2)(\widetilde{u_i}^*\widetilde{G_i} + \widetilde{u_i}\widetilde{G_i}^*)$ is the energy transfer by the nonlinear term
(iii) $\mathcal{P}_i(\boldsymbol{\kappa}, t) = -(1/2)(\widetilde{u_i}^*\widetilde{P_i} + \widetilde{u_i}\widetilde{P_i}^*)$ is the energy redistribution by pressure
(iv) $\mathcal{D}_i(\boldsymbol{\kappa}, t) = (1/2)(\widetilde{u_i}^*\widetilde{V_i} + \widetilde{u_i}\widetilde{V_i}^*)$ is the viscous dissipation
(v) $\mathcal{F}_i(\boldsymbol{\kappa}, t) = (1/2)(\widetilde{f_i}\widetilde{u_i}^* + \widetilde{f_i}^*\widetilde{u_i})$ is the work done by the IB forces (reflecting the particle–fluid interactions).

Note that in the fully developed stage, the statistical steady state is reached, so we can further compute the time average of (2.23): the time derivative vanishes, and $\mathcal{T}_i$, $\mathcal{P}_i$, $\mathcal{D}_i$ and $\mathcal{F}_i$ are in balance. For the sake of simplicity, we drop the independent variable t to denote the time-averaged energy spectra of the budget terms hereafter. Accordingly, a generic quantity $\mathcal{J}$ (which could refer to $\mathcal{E}$, $\mathcal{T}$, $\mathcal{P}$, $\mathcal{D}$ or $\mathcal{F}$) in (2.23) is a function of the three-dimensional wavenumber vector $\boldsymbol{\kappa}$. We can calculate a spherical shell integral of $\mathcal{J}(\boldsymbol{\kappa})$ to obtain a one-dimensional function (Hidman *et al.* 2023):

$$\mathcal{J}(\kappa) = \sum_{\kappa - \frac{1}{2}\Delta\kappa \leqslant \|\boldsymbol{\kappa}\| \leqslant \kappa + \frac{1}{2}\Delta\kappa} \mathcal{J}\,(\boldsymbol{\kappa})/\Delta\kappa. \tag{2.24}$$

However, the particle-induced turbulence is anisotropic under the action of gravity (see § 4). In order to further analyse the directional information of the distribution of

https://doi.org/10.1017/jfm.2025.398 Published online by Cambridge University Press

$\mathcal{J}$ in spectral space, we also calculate the average of $\mathcal{J}(\boldsymbol{\kappa})$ over the isotropic directions (on the horizontal plane), and express $\mathcal{J}$ in cylindrical coordinates (denoted by the superscript C) as

$$\mathcal{J}^C(\kappa_r, \kappa_v) = \frac{1}{N_S} \sum_{\kappa_r - \frac{1}{2}\Delta\kappa_r < \kappa_r \leqslant \kappa_r + \frac{1}{2}\Delta\kappa_r} \mathcal{J}(\boldsymbol{\kappa}) / (\Delta\kappa_r \, \Delta\kappa_v), \tag{2.25}$$

where $\kappa_v = \kappa_y$ and $\kappa_r = \sqrt{\kappa_x^2 + \kappa_z^2}$ represent the vertical and radial (along the horizontal direction) wavenumbers, respectively. The number of samples satisfying $\kappa_r - (1/2)\,\Delta\kappa_r < \kappa_r \leqslant \kappa_r + (1/2)\,\Delta\kappa_r$ is denoted by N_S, which varies with κ_r.

3. Collective behaviour of the dispersed particles

3.1. *Settling velocity*

The first observable with which we are concerned is the mean settling speed of the particles in suspension. In this study, we define the settling velocity v_s as the particle velocity along the gravitational direction, namely $v_s = -v_y$, and we use the angle bracket $\langle\cdot\rangle$ to represent the ensemble average over particles and time. In figure 2, we present the particle mean settling velocity normalized by the isolated-particle settling velocity in each case. In terms of the particle shape, the value of $\langle v_s\rangle/v_{s0}$ is greatest for oblate particles, and smallest for spherical particles, no matter whether the particles move freely or have fixed relative positions. In contrast to the decreased settling rate of spherical particles, the mean settling velocity is enhanced in the suspensions of spheroidal particles, which is in qualitative agreement with the reference data provided in figure 2. Comparing the results in the literature, we can see that the enhanced settling rate of spheroidal particles tends to increase with the non-sphericity of the particle shape. However, the degree of change in the settling velocity, measured by the ratio $\langle v_s\rangle/v_{s0}$, is reduced in the fixed relative position (FRP) cases compared to freely moving (FM) particles. The slight reduction of the mean settling velocity for spherical particles can be ascribed to the effect of hindrance (Di Felice 1999; Yin & Koch 2007). For oblate and prolate spheroids, the settling motion is further modulated by the change of particle orientation and spatial distribution in the suspension. The influence of these two effects is elaborated in the following.

3.2. *Particle orientation*

First, we examine the orientation of particles in the suspension. In figure 3, we report the statistical distribution of the particle pitch angle for the FM particles of different shapes. The results of the FRP cases are not shown since the probability density function of the particle orientation p.d.f.($|\cos\theta|$) $\equiv 1$ for particles with initially random orientation that are not allowed to rotate. As shown in figure 3, FM oblate and prolate spheroids exhibit a preferential orientation with the major axis perpendicular to the gravitational direction, i.e. $|\cos\theta| = 0$ for the prolate spheroid, and $|\cos\theta| = 1$ for the oblate spheroid. This is the stable orientation of an isolated settling spheroid under the effect of fluid inertial torque (Dabade *et al.* 2015; Ardekani *et al.* 2016), which has also been confirmed by our simulations of isolated settling oblate and prolate spheroids. The spherical particle is isotropic in shape, thus the value of $|\cos\theta|$ naturally conforms to a uniform distribution. Moreover, it is shown in figure 3 that the probability density function of the particle orientation (p.d.f.($|\cos\theta|$)) of oblate particles has a greater peak value and decays more rapidly near the peak value, than the p.d.f. of prolate spheroids. However, the tail of p.d.f.($|\cos\theta|$) is steeper for prolate particles than for oblate ones. These observations

https://doi.org/10.1017/jfm.2025.398 Published online by Cambridge University Press

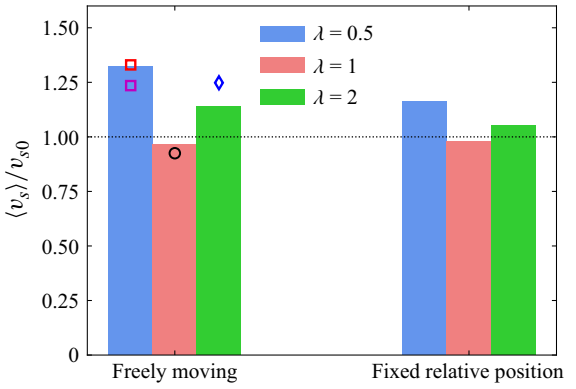


Figure 2. Mean settling velocity of the particles in suspensions in the present study (bars). Relevant results in the literature are also included for comparison (markers). Black circle: spherical particles with $\gamma = 2$, $Ga = 70$ and $\phi = 1\,\%$ (Seyed-Ahmadi & Wachs 2021). Red square: oblate particles with $\lambda = 1/3$, $\gamma = 1.02$, $Ga = 60$ and $\phi = 0.5\,\%$ (Fornari *et al.* 2018). Magenta square: oblate particles with $\lambda = 2/3$, $\gamma = 1.5$, $Ga = 110$ and $\phi = 0.5\,\%$ (Moriche *et al.* 2023). Blue diamond: prolate particles with $\lambda = 3$, $\gamma = 1.5$, $Ga = 80$ and $\phi = 1\,\%$ (Jiang *et al.* 2024*b*).

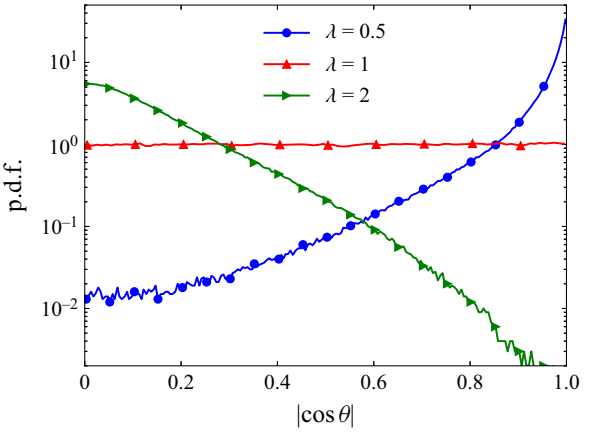


Figure 3. The p.d.f. of the absolute value of the cosine of the particle pitch angle (see figure 1 for the definition of the particle pitch angle θ).

indicate the stronger intermittency in the orientation of oblate spheroids than prolate particles under the effect of the complex particle–fluid interactions. Oblate particles show a stronger tendency to keep the stable orientation, and are also more prone to orient with the broad side aligning to the gravitational direction (i.e. $|\cos\theta| = 0$), while the opposite is true for prolate particles.

It is well known that the drag coefficient for a fixed spheroid in a uniform flow depends on the relative angle between the axis of the spheroid and the inflow direction (Zastawny *et al.* 2012; Fröhlich *et al.* 2020). Hence the settling velocity of non-spherical particles can be modulated by the change of their orientation. We note that the isolated settling velocity v_{s0} is measured for the spheroid with the broad-side-on orientation, which corresponds to the configuration with the maximum drag coefficient. Therefore, as for the spheroidal particles in the FRP cases, the randomization of the particle orientation increases the percentage of tilted particles, reducing the average drag coefficient experienced by the

https://doi.org/10.1017/jfm.2025.398 Published online by Cambridge University Press

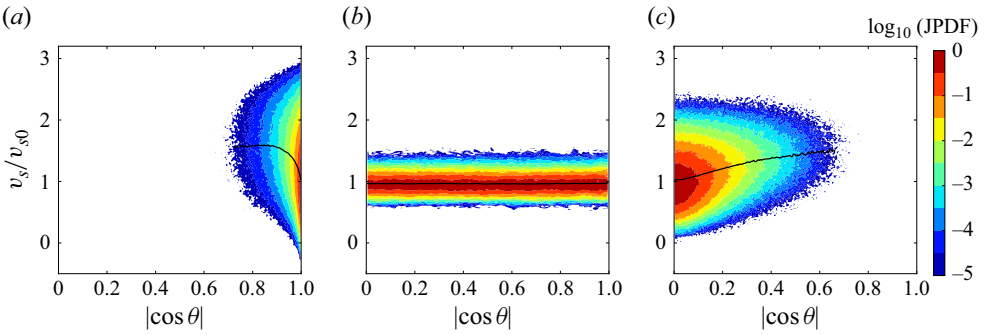


Figure 4. The joint probability density function (JPDF) (normalized by the maximum value) of the particle settling velocity and orientation. The solid lines represent the average of the settling velocity conditioned on $|\cos\theta|$ (denoted by $\langle v_s\rangle_\theta$). The data are masked when p.d.f.($|\cos\theta|$) < 0.01 max{p.d.f.($|\cos\theta|$)}.

particles. Under this effect, the mean settling velocity should increase to balance the total gravitational forces of all particles. This mechanism, which overwhelms the weak hindrance effect (in view of the low volume fraction or our suspensions), results in the enhancement of the mean settling velocity (i.e. $\langle v_s\rangle > v_{s0}$) observed for oblate and prolate particles in the FRP cases.

Regarding the cases of FM particles, we will examine the effect of particle orientation by studying the correlation between the settling velocity and the orientation of the dispersed particles. In figure 4, we depict the joint probability density function of v_s and $|\cos\theta|$ for the different particle shapes under investigation. The data show that non-spherical particles tend to accelerate the settling motion as the orientation deviates more from the broad-side-on alignment, which is consistent with the reduced drag coefficient for the isolated spheroid as θ deviates from θ_0. Specifically, the conditionally averaged settling velocity, denoted by $\langle v_s\rangle_\theta$, increases rapidly as $|\cos\theta|$ deviates from 1 for oblate spheroids, while the variation of $\langle v_s\rangle_\theta$ is moderate for prolate spheroids with the changing $|\cos\theta|$. These trends are similar to that of the variation of p.d.f.($|\cos\theta|$) near θ_0 displayed in figure 3. However, it is noteworthy from figure 2 that the mean settling velocity for FM spheroids is much larger than that for FRP particles, although the particle orientations in the latter cases are farther from the broad-side-on alignment (the maximum-drag orientation) than in the former cases. This indicates that the enhancement of the mean settling velocity for FM spheroidal particles cannot be solely ascribed to the change of orientation. In what follows, we therefore investigate the effect of the spatial distribution on the settling motion of the FM particles.

3.3. *Particle clustering*

3.3.1. *Visualization of the flow and the particle pair correlation*

Initially, we provide visualizations of the instantaneous three-dimensional flow fields together with the dispersed particles for the FM cases in figure 5. One can observe large-scale fluid structures in the suspensions with non-spherical particles, illustrated by the iso-surface of the vertical fluid velocity, $u_y = -v_{s0}$. These flow structures, extending vertically across the whole computational domain, are the footprints of column-like particle clusters. The case with spherical particles, however, is characterized by the small-scale wakes of spheres settling almost in isolation, as shown in figure 5(*b*). In previous studies, researchers have linked the formation of particle clusters to the wake-induced hydrodynamic interactions among settling particles, which is the same mechanism behind the DKT process for a pair of settling particles (see, among others, Zaidi *et al.* 2014;

https://doi.org/10.1017/jfm.2025.398 Published online by Cambridge University Press

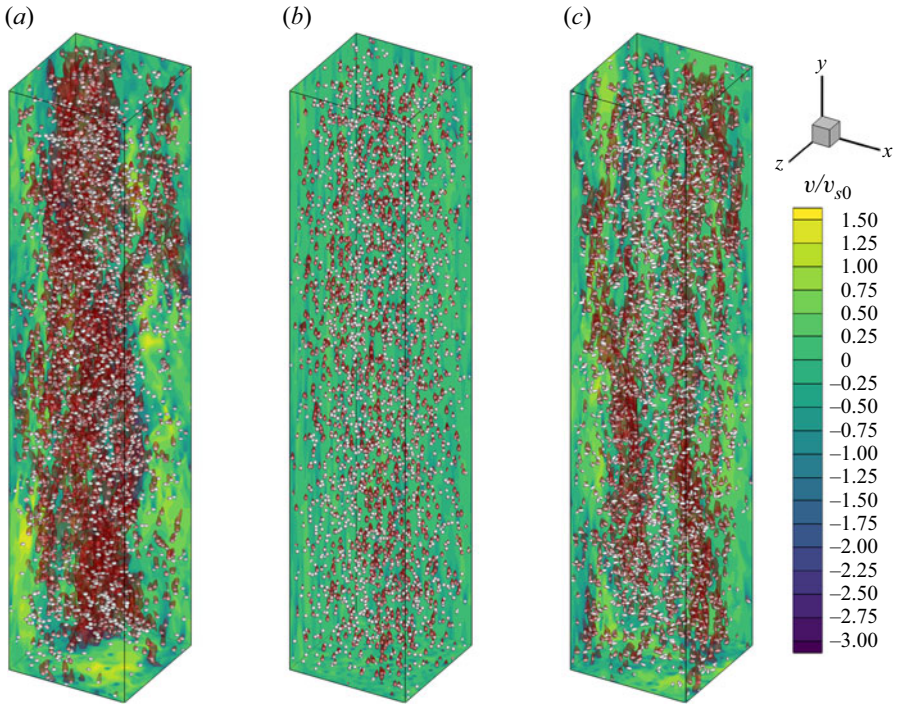


Figure 5. Snapshots of the vertical velocity of the fluid flow and particle distribution in the FM cases for (*a*) oblate particles, (*b*) spherical particles and (*c*) prolate particles. The iso-surfaces in red represent the vertical fluid velocity with $u_y = -v_{s0}$. Particle surfaces are depicted in grey.

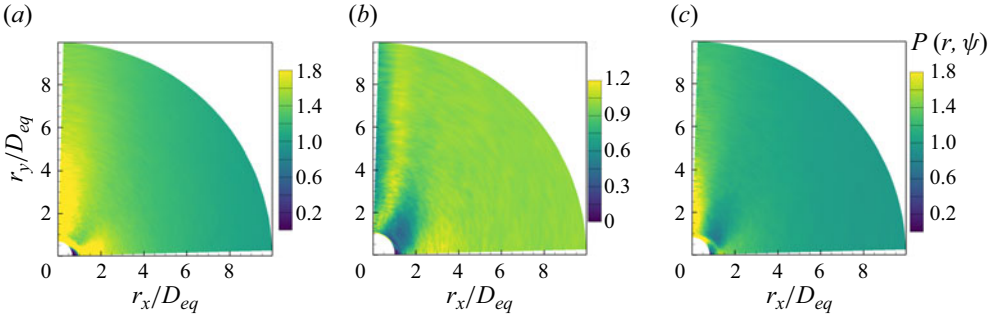


Figure 6. Pair correlation functions $P(r, \psi)$ from the simulations of FM particles for (*a*) oblate spheroids, (*b*) spherical particles and (*c*) prolate particles.

Fornari *et al.* 2018). As for spherical particles, the absence of particle clusters in the current simulation is explained by the weak intensity of the particle wakes due to the relatively low settling Reynolds number (Zaidi *et al.* 2014); the stronger wake-induced hydrodynamic interactions occurring for spheroidal particles (Ardekani *et al.* 2016; Moriche *et al.* 2023) are responsible for the emergence of clustering in the suspensions of oblate/prolate particles observed in figure 5(*a*,*c*).

To better understand the micro-structure of the particles in the suspension, we examine the spatial correlation of the dispersed phase. Figure 6 illustrates the two-dimensional pair correlation function $P(r, \psi)$ (for the definition, see Yin & Koch 2007; Fornari *et al.* 2018),

https://doi.org/10.1017/jfm.2025.398 Published online by Cambridge University Press

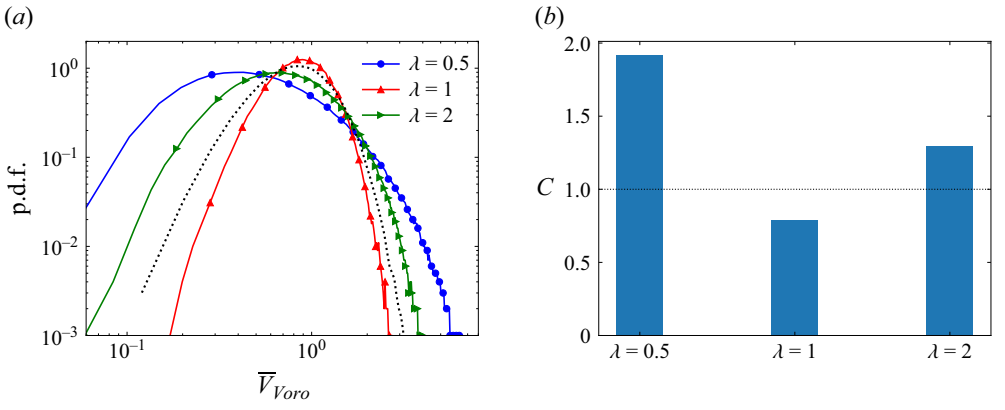


Figure 7. Voronoi analysis of the spatial distribution of FM particles. (*a*) The p.d.f. of the normalized Voronoi volumes. The dotted line illustrates the p.d.f. associated with a random distribution of spherical particles for comparison. (*b*) Clustering indicator for particles with different shapes.

for the particles with different shapes. The function $P(r, \psi)$ estimates the probability of finding particle pairs with separation (r_x, r_y) (or equivalently, (r, ψ) in spherical coordinates), in which $r_x = r\cos\psi$ and $r_y = r\sin\psi$ represent the horizontal and vertical distances between two particles. The value of $P(r, \psi)$ is larger than 1 if the probability of finding a particle pair with separation (r, ψ) is higher than for randomly distributed particles, whereas $P(r, \psi) < 1$ indicates regions depleted of particles.

As shown in figure 6(*a*,*c*), the value of $P(r, \psi)$ is greater than unity for close-by particles along the vertical direction, indicating vertical arrangements of settling oblate/prolate particles in the suspension. This observation is consistent with the column-like particle clusters displayed in figure 5(*a*,*c*). Moreover, the value of $P(r, \psi)$ decays slowly as the separation distance r increases along the vertical direction, especially for oblate particles, which is in agreement with the finding of settling low-aspect-ratio oblate particles by Moriche *et al.* (2023). These authors argue that the particle clusters can continuously grow to a size as large as the entire periodic computational domain, once the dispersed particles start to attract each other by DKT-like interactions. However, as shown in figure 6(*b*), the vertically aligned particle micro-structures are absent for non-clustering settling spheres. Instead, we observe a region devoid of particles at the separation distance $r \lesssim 2D_{eq}$ within the range of azimuthal angle $40° \lesssim \psi \lesssim 70°$. This void region is also accompanied by a relatively high particle correlation along the horizontal direction, similar to the observations reported in Yin & Koch (2007) and Shajahan & Breugem (2023). We attribute the presence of the void region to the rapid tumbling and separation of particle pairs during the DKT-like events. After that, particle pairs separate and form horizontally aligned pairs that enhance the particle correlation in the horizontal direction (Yin & Koch 2007).

3.3.2. *Voronoi analysis*

Next, we conduct a Voronoi analysis to quantify the clustering of the dispersed particles (Monchaux *et al.* 2010). We report the p.d.f. of the normalized Voronoi volumes in figure 7(*a*) for the FM cases with different particle shapes. It is observed that the probability of finding Voronoi tessellations with small and large volumes is significantly higher for non-spherical particles, especially for oblate spheroids, than for spherical particles. This indicates an increased percentage of volumes with close-by particles,

https://doi.org/10.1017/jfm.2025.398 Published online by Cambridge University Press

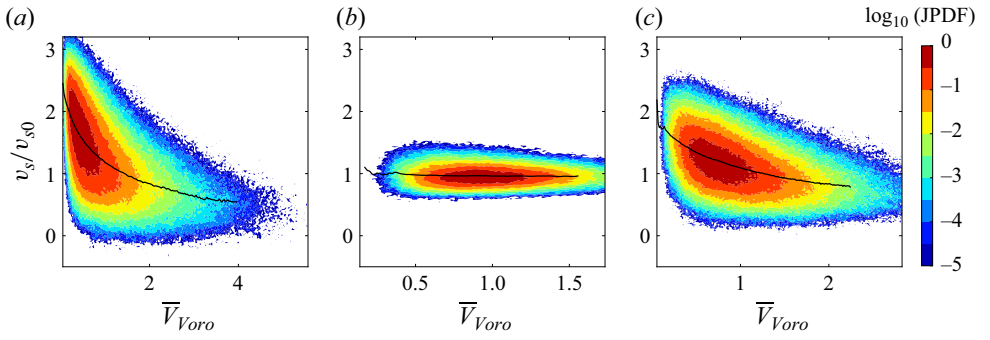


Figure 8. The joint probability density function (JPDF) of the particle settling velocity and the normalized Voronoi volume in the FM cases with (*a*) oblate particles, (*b*) spherical particles and (*c*) prolate particles. The solid lines represent the average settling velocity conditioned on the normalized Voronoi volume (the data are masked when p.d.f.$(\overline{V}_{Voro}) < 0.001$ max(p.d.f.$(\overline{V}_{Voro})$)).

as well as voids, in suspensions of non-spherical particles, which is a sign of particle clustering (Monchaux *et al.* 2010). The clustering indicator C (see (2.19) for its definition) shown in figure 7(*b*) also confirms the morphology of clustering for non-spherical particles ($C > 1$). In particular, in the suspension of oblate particles, the standard deviation of the normalized Voronoi volume is greater than that of a random distribution by more than 90 %. The significant clustering of oblate particles can be related to the stable piled-up configuration of pairwise oblate spheroids during the DKT process (Ardekani *et al.* 2016; Fornari *et al.* 2018). In contrast, the p.d.f. of $\overline{V}_{Voro}$ is narrow, and the value of C is lower than unity for spherical particles. The deviation from the random spatial distribution for spherical particles is related to the horizontally aligned particle micro-structures observed in figure 6(*b*).

To gain further insights, we investigate the correlation between the particle settling motion and the particle clustering. We therefore illustrate the joint probability density function of the settling velocity and Voronoi volume for the FM particles of different shapes in figure 8. Interestingly, in the cases with significant particle clustering (oblate/prolate particles; see figure 8*a*,*c*), we can observe an evident negative correlation between v_s and $\overline{V}_{Voro}$. In other words, particles tend to settle faster in the regions where the local concentration is higher, and vice versa. This can be interpreted by the preferential sampling of downward wake flows by the locally accumulated particles (corresponding to small values of $\bar{V}_{Voro}$) (Uhlmann & Doychev 2014; Jiang *et al.* 2024*b*). As a consequence, a cluster of particles experiences a smaller total hydrodynamic drag than the sum of the drag of the same number of isolated particles (Koch & Hill 2001; Dodds *et al.* 2020). On the contrary, in the regions depleted of particles (i.e. for large values of $\bar{V}_{Voro}$), the settling velocity is reduced to less than that of an isolated particle due to the effect of hindrance (Di Felice 1999). However, for spherical particles, the correlation between v_s and $\overline{V}_{Voro}$ becomes less pronounced (see figure 8*b*), which can be attributed to the orderly arrangement of settling spheres in space. According to the above discussion, it is not surprising that the mean settling velocity of the dispersed particles is highly correlated to the degree of particle clustering, which can be identified by comparing figure 2 with figure 7(*b*). Similar findings were also reported in the studies by Uhlmann & Doychev (2014) and Moriche *et al.* (2023) about the sedimentation of particles with different Galileo numbers and shapes.

https://doi.org/10.1017/jfm.2025.398 Published online by Cambridge University Press

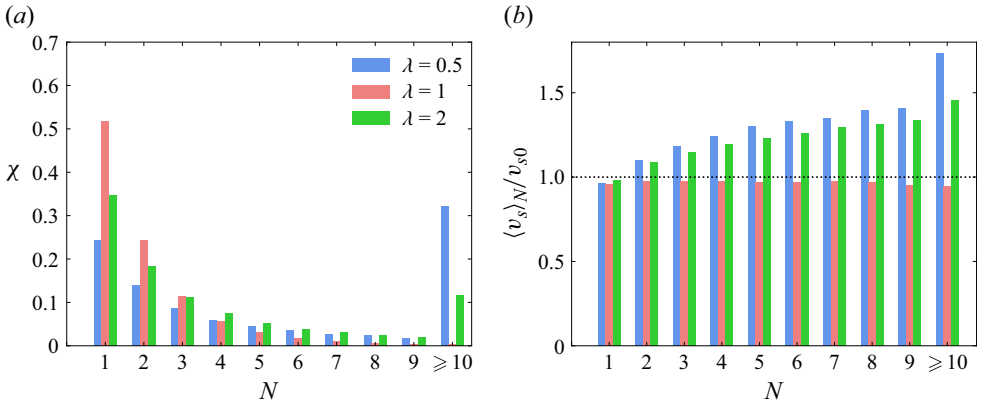


Figure 9. (*a*) The fraction of the total number of particles forming clusters with N particles. (*b*) The averaged settling velocity of the particles within clusters of different sizes.

3.3.3. *Size of particle clusters*

To deepen the analysis, we also estimate the sizes of clusters in the FM cases with different particle shapes. Specifically, we regard two particles as part of the same cluster if their centre-to-centre distance, denoted by d_{cc}, satisfies $d_{cc} < 0.5\phi^{-1/3}D_{eq}$. The factor $\phi^{-1/3}$ is included in the definition to consider the effect of volume fraction, as the mean distance between two neighbouring particles decays with $\phi^{-1/3}$ in a particle assembly. We define the size of particle clusters by the number of member particles N, with $N = 1$ indicating an isolated particle (see, among others, Fornari *et al.* 2018). In figure 9, we present the fraction of the total particle number (denoted by χ) and the averaged settling velocity (denoted by $\langle v_s\rangle_N$) in clusters with different sizes. As shown in figure 9(*a*), oblate particles are most prone to form large-size clusters, with more than 30 % of the particles being found in clusters with $N \geqslant 10$. In contrast, the percentage of isolated spherical particles ($N = 1$) is considerably higher than that of non-spherical particles, and clusters with $N > 5$ are very seldom found for settling spheres. Regarding the settling velocity, it is indicated by figure 9(*b*) that the non-spherical particles pertaining to the clusters with the larger size tend to settle more rapidly; however, $\langle v_s\rangle_N$ becomes almost independent of the cluster size for spherical particles. These observations are in qualitative agreement with the results shown in figure 8 on the Voronoi analysis, and further confirm the significance of clustering on the particle settling velocity in the suspension.

4. Particle-induced turbulence

In this section, we will examine the pseudo-turbulence induced by the settling particles, following the denomination used for turbulence induced by rising bubbles, to which we will compare the present results.

4.1. *One-point statistics of the fluid velocity fluctuations*

We start with the one-point statistics of the fluid velocity fluctuations in the particle-induced turbulent flows. Here, the fluid velocity fluctuation is defined by $u_i' = u_i - \langle u_i\rangle_f$, in which $\langle\cdot\rangle_f$ denotes the average within the domain occupied by the fluid phase. For the present flow system, the two horizontal velocity components (along the x and z directions) are statistically equivalent with zero mean velocity (i.e. $\langle u\rangle_f = \langle w\rangle_f = 0$), while there is a mean upward flow along the vertical direction, with $\langle v\rangle_f = \phi\langle v_s\rangle/(1-\phi)$ to maintain

https://doi.org/10.1017/jfm.2025.398 Published online by Cambridge University Press

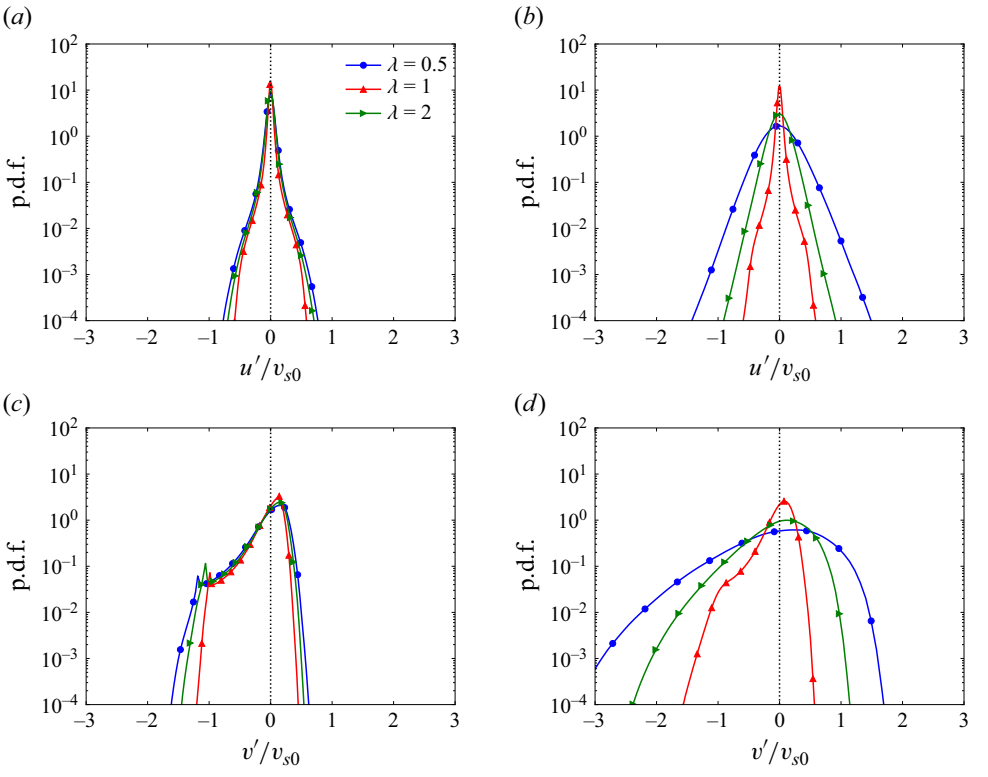


Figure 10. Probability density functions of the fluctuations of (*a,b*) the horizontal fluid velocity, and (*c,d*) the vertical fluid velocity: (*a,c*) simulations of FRP particles; (*b,d*) simulations of FM particles.

the zero flux of the whole system (Yin & Koch 2007). In figure 10, we present p.d.f.s of the fluctuations of the horizontal and vertical fluid velocities for each case under consideration. It is shown that the horizontal velocity fluctuation exhibits a symmetric distribution, while the p.d.f. of v' is skewed with a slow decay for the negative tail. This observation is the result of downward wake flow behind settling particles, resembling the statistical distribution of the velocity fluctuations in bubble-induced pseudo-turbulence (Riboux *et al.* 2010). Considering the cases with FRP particles, the shape effect on the p.d.f.s is marginal. The horizontal velocity fluctuation is highly localized around $u' = 0$, with a pronounced peak. On the other hand, the p.d.f. of v' exhibits a secondary peak at $v' \approx -v_{s0}$, which can be interpreted by the identical settling velocity for all the dispersed particles in this scenario.

In contrast, the statistical distribution of the fluid velocity fluctuation exhibits greater shape dependency in the cases with FM particles. The p.d.f.s of u' and v' for spherical particles are similar to those of the FRP case, but they are significantly broader, with a longer negative tail in the cases with oblate and prolate particles (see figure 10*c*,*d*). These observations are quantified by the root mean square and the skewness of the velocity fluctuations provided in table 2. As a matter of fact, the oblate/prolate particles exhibit stronger horizontal motions than spherical particles (not shown here) because of the lateral drift of settling spheroids with inclined orientations (Jiang *et al.* 2024*c*). This mechanism results in enhanced fluctuations of the horizontal fluid velocity in the corresponding cases. Moreover, the fluid flows in the regions surrounded with particle clusters (dominated by downward wake flows) and voids (dominated by upward mean flows) contribute differently

https://doi.org/10.1017/jfm.2025.398 Published online by Cambridge University Press

	$\lambda = 0.5$ (FRP)	$\lambda = 1$ (FRP)	$\lambda = 2$ (FRP)	$\lambda = 0.5$ (FM)	$\lambda = 1$ (FM)	$\lambda = 2$ (FM)
u'_{rms}/v_{s0}	0.063	0.042	0.057	0.25	0.046	0.14
v'_{rms}/v_{s0}	0.26	0.20	0.24	0.64	0.21	0.42
$S(v')$	−1.678	−1.890	−1.842	−0.622	−1.667	−0.732
R	4.15	4.80	4.30	2.57	4.54	3.01

Table 2. Quantification of the fluid velocity fluctuations. The subscript rms here represents the root mean square. The skewness of the vertical velocity fluctuation is denoted by $S(v')$. The ratio $R = v'_{rms}/u'_{rms}$ is used to measure the flow anisotropy.

to the vertical fluid velocity, giving rise to the enhanced vertical velocity fluctuations for the cases with non-spherical particles, in particular oblate particles when clustering is most prominent. In addition, although the prevalence of particle clusters intensifies the downward fluid flow (with the increased probability to observe negative v' of large magnitude), the disappearance of the local peak of the p.d.f. at $v' \approx -v_{s0}$ explains the reduced skewness $S(v')$ in the cases with FM oblate/prolate particles.

In table 2 we also report the ratio between the root mean square values of the vertical and horizontal velocity fluctuations. We use this quantity to measure the anisotropy of the current fluid flows. Basically, the results show that the value of v'_{rms}/u'_{rms} is always greater than unity, indicating stronger fluctuations in the vertical velocity component. However, it is interesting to note a significantly lower flow anisotropy in the cases with FM oblate/prolate particles compared with other cases. We will discuss the correlation between this observation with the particle clustering in § 4.2.2.

4.2. *Energy spectra and scale-by-scale budget of the particle-induced turbulence*

4.2.1. *Total energy analysis*

In what follows, we perform a spectral analysis of the pseudo-turbulence induced by settling particles. Referring to the derivation in § 2.4.2, we obtain the scale-by-scale budget of the turbulence kinetic energy (TKE) in spectral space by taking the summation over index i in (2.23):

$$\frac{\partial \mathcal{E}_k(\boldsymbol{\kappa})}{\partial t} = \mathcal{T}_k(\boldsymbol{\kappa}) + \mathcal{P}_k(\boldsymbol{\kappa}) + \mathcal{D}_k(\boldsymbol{\kappa}) + \mathcal{F}_k(\boldsymbol{\kappa}). \tag{4.1}$$

Here, the subscript k represents the TKE, and a generic term $\mathcal{J}_k(\boldsymbol{\kappa})$ in (4.1) is defined as $\mathcal{J}_k(\boldsymbol{\kappa}) = \sum_{i=1,2,3} \mathcal{J}_i(\boldsymbol{\kappa})$, where $\mathcal{J}$ could be $\mathcal{E}$, $\mathcal{T}$, $\mathcal{P}$, $\mathcal{D}$ or $\mathcal{F}$. Accordingly, the TKE is the summation of $\mathcal{E}(\boldsymbol{\kappa})$ over all wavenumbers, i.e.

$$k = \frac{1}{2}\left\langle u^2 + v^2 + w^2 \right\rangle = \sum_{\boldsymbol{\kappa}} \mathcal{E}_k(\boldsymbol{\kappa}). \tag{4.2}$$

Similarly, the total dissipation rate can be related to $\mathcal{D}(\boldsymbol{\kappa})$ by

$$\varepsilon = -2\nu\langle s_{ij}s_{ij}\rangle = \sum_{\boldsymbol{\kappa}} \mathcal{D}_k(\boldsymbol{\kappa}), \tag{4.3}$$

where s_{ij} denotes the tensor of the velocity deformation rate. The term $\mathcal{F}_k$ in (4.1) represents the work associated with the IB forces, which reflects the particle–fluid interactions. Note that the gravitational potential energy of the settling particles is injected into the fluid flow via IB forces. Hence $\mathcal{F}_k$ serves as the energy production of the fluid flow, and we have the relationship $\sum_{\boldsymbol{\kappa}} \mathcal{F}_k(\boldsymbol{\kappa}) = -\varepsilon$ in the steady state. As we will show below,

https://doi.org/10.1017/jfm.2025.398 Published online by Cambridge University Press

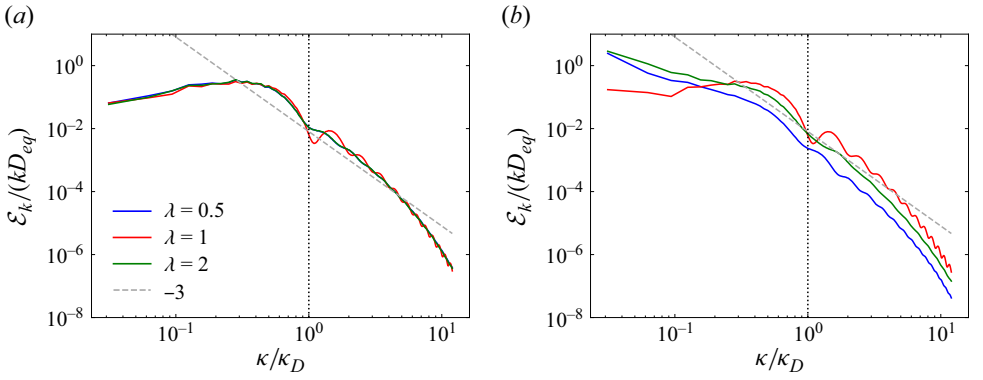


Figure 11. Energy spectra versus the wave vector magnitude for all cases under consideration: (*a*) FRP particles, (*b*) FM particles. The dotted vertical line represents the wavenumber corresponding to the particle equivalent diameter, i.e. $\kappa_D = 2\pi/D_{eq}$.

the work done by IB forces inputs energy in the fluid flow over a broad range of scales, not only at the largest ones as in the classic homogeneous isotropic turbulence. Also, this energy production varies among the different cases, and is related to the different flow and particle structures in the current system.

To begin with, we report in figure 11 the spherical shell integral of the energy spectra, i.e. the energy as a function of the wave vector magnitude $\kappa = \|\boldsymbol{\kappa}\|$, for all cases under consideration. First, we observe in figure 11(*a*) that the energy spectra, normalized by the TKE, almost collapse for all the FRP cases, despite the different particle shapes. The only difference is that the oscillation of the energy spectra at $\kappa \gtrsim \kappa_D$ is more severe for settling spheres. This kind of oscillation is caused by the presence of dispersed particles in the fluid due to the so-called 'boxcar effect' (Lucci *et al.* 2010). According to the quantitative analysis by Lucci *et al.* (2010) and Ramirez *et al.* (2024), the period of the oscillation $T_{osci} = 2\pi/D$ corresponds to the diameter of spherical particles. Our results in figure 11 are in agreement with this theory. Additionally, the oscillations of the energy spectra are damped for the cases with spheroidal particles, since oscillation periods varying between $2\pi/D_{max}$ and $2\pi/D_{min}$ (where D_{min} and D_{max} represent the minor and major axes of the spheroid) cancel each other out (Ramirez *et al.* 2024). Similar oscillations were also reported in the energy spectra of particle-laden homogeneous isotropic turbulence, and have negligible effect on the physical interpretation of the results (Wang *et al.* 2014; Chiarini & Rosti 2024). For the cases with FM particles, however, figure 11(*b*) demonstrates that more energy is contained at large scales for the flows with oblate/prolate spheroids than for spherical particles. This observation is related to the large-scale flow structures accompanied by the large-scale particle clusters shown in figure 5. Moreover, we can clearly observe a κ^{-3} decay for the energy spectra at scales comparable to or smaller than the particle size, regardless of the particle shape and motion type (FM or FRP). This power law of the energy spectra has been widely reported in previous studies on bubble-induced pseudo-turbulence (Lance & Bataille 1991; Riboux *et al.* 2010; Roghair *et al.* 2011; Risso 2011). In Lance & Bataille (1991), the κ^{-3} power law of the energy spectra was originally explained by the assumption of a local balance between the energy production (estimated by $\kappa^{-1}\varepsilon_w$, where ε_w is the viscous dissipation in the wake) and the dissipation ($\mathcal{D}(\kappa) = -2\nu\kappa^2\,\mathcal{E}(\kappa)$) on the corresponding scales. Note, however, that a similar power law was also observed for bubble-induced turbulence in Pandey *et al.* (2020)

https://doi.org/10.1017/jfm.2025.398 Published online by Cambridge University Press

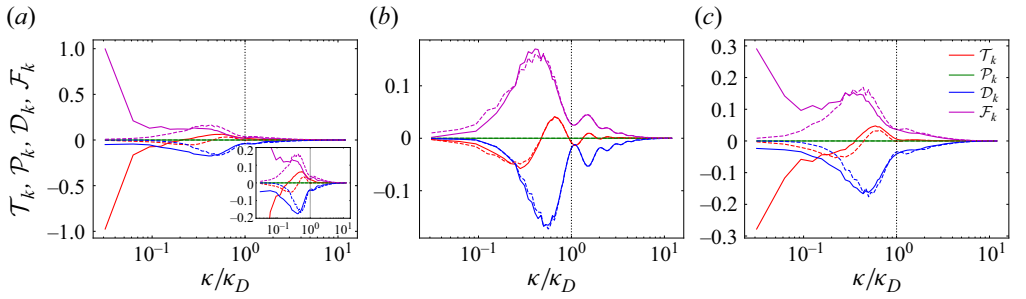


Figure 12. Spherical integral of the budget terms (each term is normalized by εD_{eq}) of the TKE for: (*a*) oblate particles, (*b*) spherical particles and (*c*) prolate particles. The solid lines represent the FM cases, while the dashed lines correspond to the FRP cases. The inset in (*a*) depicts a zoomed-in view of the data in the same figure with a reduced range of the vertical axis. The dotted vertical line in each plot represents the wavenumber $\kappa = \kappa_D$.

and Zamansky *et al.* (2024), where the viscous dissipation is seen to balance both nonlinear transfer and turbulence production by the interphase coupling.

To examine the aforementioned assumption in the current configurations, we further investigate the energy budget in the particle-induced turbulent flows. To this end, we compute the scale-by-scale budgets of the TKE, and report the contribution from each term on the right-hand side of (4.1) in figure 12. Note that the term related to pressure, $\mathcal{P}_k$, vanishes because of the incompressible constraint of the flow. As a feature common to all cases, the energy transfer by the nonlinear terms, $\mathcal{T}_k$, is acting primarily on scales larger than the particle size. At smaller scales with $\kappa \gtrsim \kappa_D$, the contribution of $\mathcal{T}_k$ decays faster than $\mathcal{F}_k$ and $\mathcal{D}_k$. Within this range of wavenumbers, the work done by the IB forces approximately balances the viscous dissipation, i.e. $\mathcal{F}_k(\kappa) \approx -\mathcal{D}_k(\kappa)$. Our results show therefore that the idea proposed by Lance & Bataille (1991) regarding the local balance between interphase energy transfer and viscous dissipation applies also to the case of particle sedimentation. Note, however, that unlike the case of deformable bubbles where dissipation is found in the wakes, viscous dissipation in suspensions of settling rigid spheres is expected to occur in the near-boundary regions on the front and lateral sides of the particles; see figure 8 in Fornari *et al.* (2016). By virtue of the dimensional analysis, the energy input by the IB forces can be estimated by $\mathcal{F}_k \sim \kappa^{-1}\varepsilon_{sl}$ (with ε_{sl} representing the viscous dissipation in the shear layer near the particle surfaces) on these small scales, since the energy injection by gravity contributes mainly to the energy budget on the scales larger than the dispersed phase (Pandey *et al.* 2020; Ramirez *et al.* 2024). As a consequence, we arrive at the κ^{-3} scaling law of the energy spectra by considering the balance $\mathcal{F}_k(\kappa) \approx -\mathcal{D}_k(\kappa)$. Additionally, a similar local balance for the flow budget was also reported in homogeneous shear turbulence laden with sub-Kolmogorov particles (Gualtieri *et al.* 2013, 2017). However, the local energy input due to the feedback from the tiny particles was shown to scale with κ^{-2} at scales $\kappa\eta \approx 1$ (with η being the Kolmogorov length scale), leading to a κ^{-4} power law of the energy spectrum (Gualtieri *et al.* 2017), whereas in the numerical model by Le Roy De Bonneville *et al.* (2021) and Zamansky *et al.* (2024), although the interface is not resolved, interactions between bubble wakes are. This leads to the κ^{-3} scaling of the energy spectra, similar to the case of large bubbles or particles. These authors attributed this scaling to the mean shear rate imposed by the bubbles, which controls the rate of return to isotropy. We therefore conjecture that two-way coupling approaches not modelling wake interactions can be relevant only at low volume fractions or for very small particles.

https://doi.org/10.1017/jfm.2025.398 Published online by Cambridge University Press

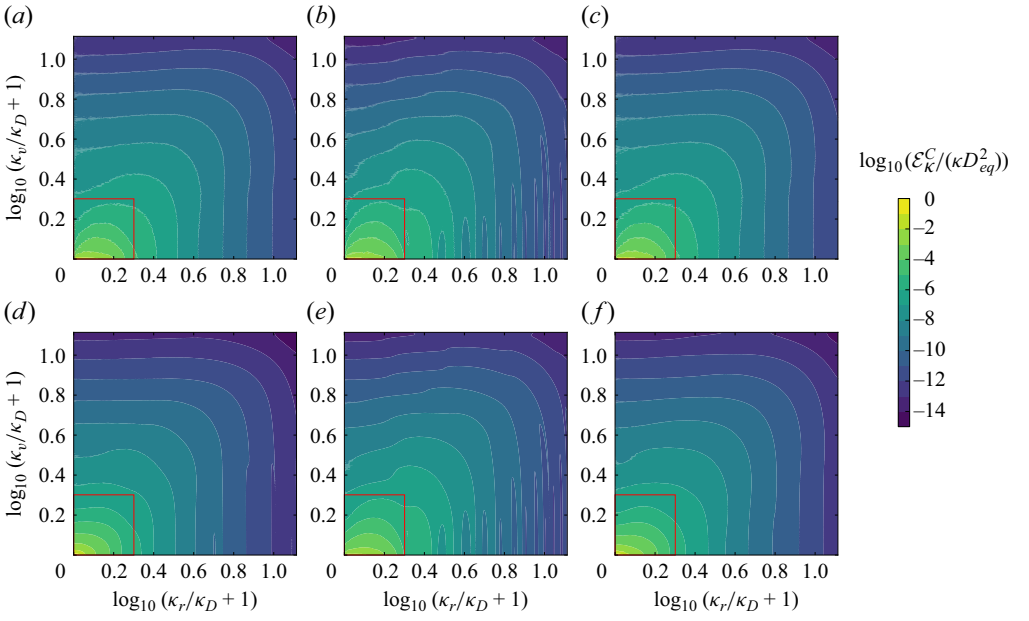


Figure 13. Distribution of the energy spectra in cylindrical coordinates ($\mathcal{E}_k^C$) in the spectral space for (*a–c*) the FRP cases and (*d–f*) the FM cases, for (*a,d*) oblate particles, (*b,e*) spherical particles and (*c,f*) prolate particles. The red lines highlight the wavenumbers corresponding to the particle size, i.e. $\kappa_r = \kappa_D$ and $\kappa_v = \kappa_D$.

Let us now move to the large scales where the energy injection due to gravity dominates. It is noteworthy from figure 12 that the work done by the IB forces, $\mathcal{F}_k$, exhibits a striking peak at the smallest wavenumber in the cases of FM spheroidal particles. As discussed in § 3.3, settling oblate or prolate particles tend to form column-like clusters whose scale could become comparable to the entire computational domain (Moriche *et al.* 2023). Consequently, energy is injected into the flow primarily by the interaction between the fluid flow and these large-scale particle clusters. This mechanism is also responsible for the rise of energy spectra $\mathcal{E}_k$ at small wavenumbers in the FM cases with oblate/prolate particles (see figure 11*b*), corresponding to the large-scale flow structures displayed in figure 5(*a*,*c*). Moreover, we also notice that the magnitude of the peak value of $\mathcal{F}_k$ on a large scale is correlated to the degree of particle clustering, and vanishes when the particle clustering is absent or not allowed.

To gain further understanding about the characteristics of the particle-induced pseudo-turbulence, we now examine the spectra of TKE and its budget in cylindrical coordinates in spectral space, as introduced in § 2.4.2. First, we depict the two-dimensional maps of $\mathcal{E}_k^C$ in the $\kappa_r - \kappa_v$ plane in figure 13 (refer to (2.25) for its definition). Compared to the spherical integral of the energy spectra presented in figure 11, the energy density represented by $\mathcal{E}_k^C$ additionally provides directional information for the distribution of TKE in the spectral space. We will note that for the single-phase homogeneous isotropic turbulence, the isotropic distribution of energy yields contour lines of $\mathcal{E}_k^C$ that are symmetric about the diagonal line in the $\log \kappa_r - \log \kappa_v$ plane (not shown here). For the particle-induced pseudo-turbulence, instead, we observe in figure 13 that the energy spectra decay more rapidly along the vertical than the horizontal direction. This kind of anisotropy is mainly exhibited at scales larger than the particle size, seemingly due to the flow structures induced by the particle settling motion. In the horizontal direction, thin shear layers exist besides

https://doi.org/10.1017/jfm.2025.398 Published online by Cambridge University Press

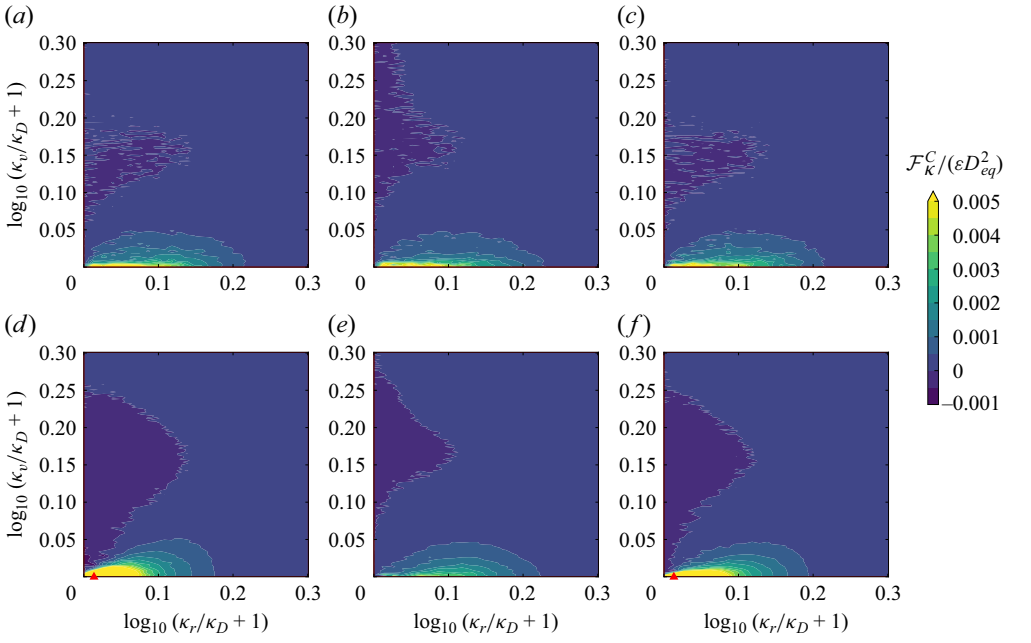


Figure 14. Distribution of the work done by the IB force in cylindrical coordinates ($\mathcal{F}_k^C$) in the spectral space for (*a–c*) the FRP cases and (*d–f*) the FM cases, for (*a,d*) oblate particles, (*b,e*) spherical particles and (*c,f*) prolate particles. For clarity, we display only the results at large scales with $\kappa_r \leqslant \kappa_D$ and $\kappa_v \leqslant \kappa_D$. The red triangle in (*d,f*) corresponds to the wavenumber $(\kappa_r, \kappa_v) = (2\pi/L_x, 0)$.

the downward-moving particles, which are reflected by the energy at high horizontal wavenumber κ_r. In contrast, the flow structures are elongated in the vertical direction (including the particle wakes or the streaks of upcoming fluid on their side), corresponding to more energy at low vertical wavenumbers κ_v. Interestingly, this anisotropy is less prominent for the flows induced by FM non-spherical particles, although the column-like particle clusters are longer in these cases. This will be discussed further when commenting on figure 15 about the role of the nonlinear energy transfer among scales. Finally, at small scales (great values of κ_r and κ_v), the energy spectra $\mathcal{E}_k^C$ progressively recover isotropy.

In figures 14–16, we illustrate the scale-by-scale budget terms of TKE (except for the vanishing term $\mathcal{P}_k^C$) in cylindrical coordinates (visualized on the $\kappa_r - \kappa_v$ plane). Incidentally, we display only the data with low wavenumbers, i.e. $\kappa_r < \kappa_D$ and $\kappa_v < \kappa_D$, since the budget terms decay rapidly and recover the isotropic distribution on small scales. Considering first the term $\mathcal{F}_k^C$, the results shown in figure 14 indicate that the IB forces do work and inject energy at large scales in the vertical direction (low wavenumbers κ_v); moreover, we observe that positive values of $\mathcal{F}_k^C$ cover a wider range of scales in the horizontal direction. Notably, in the cases of FM non-spherical particles, a striking peak of $\mathcal{F}_k^C$ is observed at the smallest values of κ_v, which may be related to the particle clusters extending across the whole computational domain in the periodic vertical direction with a lateral span comparable to the horizontal domain size (Moriche *et al.* 2023). As a consequence, the peak value of $\mathcal{F}_k^C$ corresponds to the wavenumbers $\kappa_v = 0$ and $\kappa_r = 2\pi/L_x$ in the FM cases of oblate/prolate particles, and is less sharp along the horizontal direction than the vertical direction. For the cases where particle clustering is absent, the aforementioned peak becomes less pronounced.

https://doi.org/10.1017/jfm.2025.398 Published online by Cambridge University Press

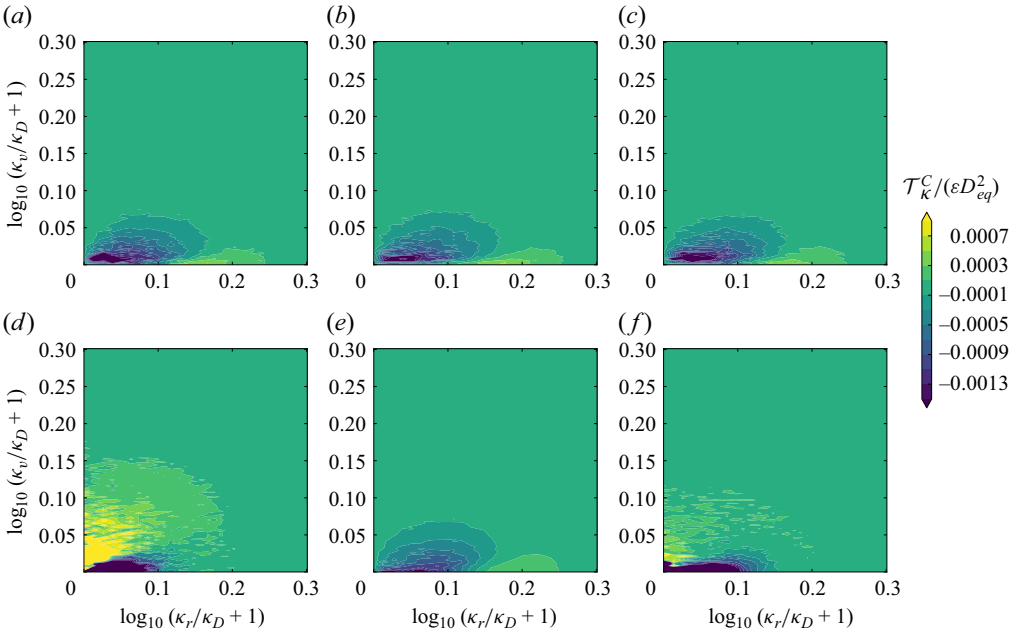


Figure 15. Same as figure 14, but for the nonlinear transfer spectra $\mathcal{T}_k^C$.

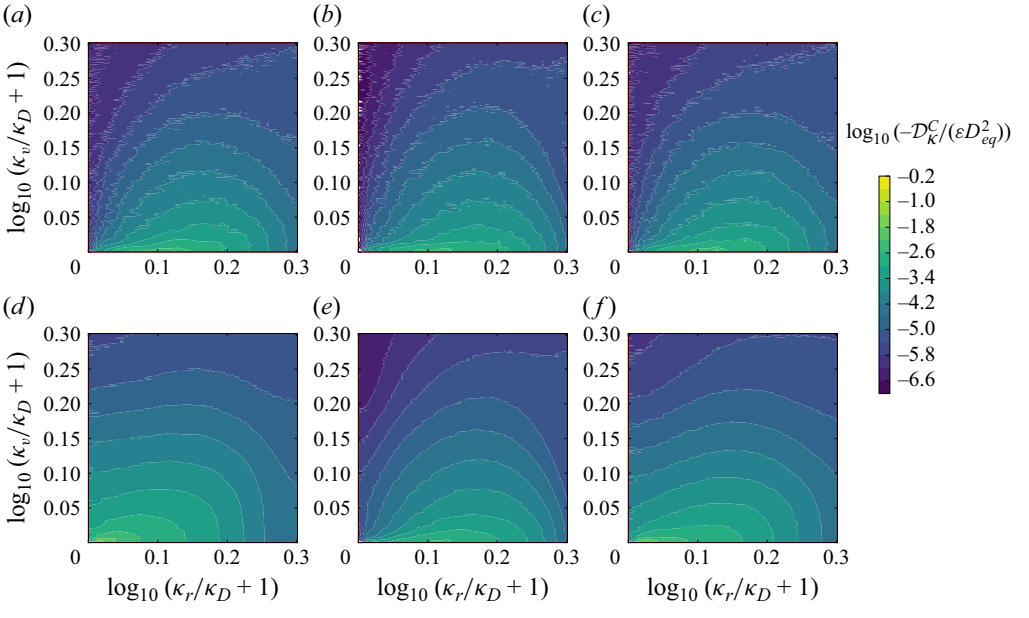


Figure 16. Same as figure 14, but for the viscous dissipation spectra $\mathcal{D}_k^C$.

Next, the effect of the nonlinear transfer is illustrated in figure 15. It is demonstrated that the energy is transferred by the nonlinear interactions not only between different radial scales (quantified by the term $\mathcal{T}_k(\kappa)$ in figure 12), but also in a more complex way along the azimuthal direction on the $\kappa_r - \kappa_v$ plane. Overall, we notice that the energy input by the fluid–particle interaction forces (corresponding to the peak value of $\mathcal{F}_k^C$ shown in

https://doi.org/10.1017/jfm.2025.398 Published online by Cambridge University Press

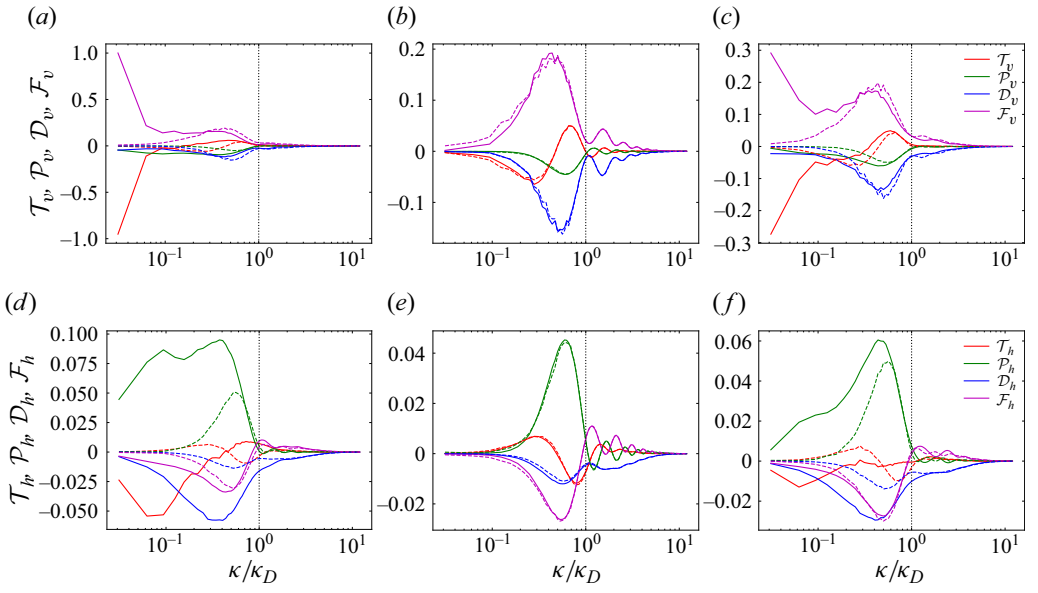


Figure 17. Budget terms of (*a–c*) the vertical component and (*d–f*) the horizontal component of TKE, for (*a,d*) oblate particles, (*b,e*) spherical particles and (*c,f*) prolate particles. The solid lines represent the FM cases, while the dashed lines represent the FRP cases.

figure 14) is efficiently transferred to the close regions near the κ_v axis (which is most clear by the positive peak of $\mathcal{T}_k^C$ in figure 15*d*). This process appears to be more significant in the suspensions of FM spheroidal particles. As a result, the anisotropic distribution of turbulence kinetic energy on the $\kappa_r-\kappa_v$ plane is more clearly mitigated for the flow of settling oblate/prolate particles than for the spherical ones (see figure 13), although the energy input exhibits stronger anisotropy in the non-spherical cases, as displayed in figure 14. We conjecture that this more efficient transfer in the presence of clustering might be due to the meandering of the particle-depleted regions and to the stronger wake–wake interactions in the clustering regions.

Finally, it is shown in figure 16 that the viscous dissipation $\mathcal{D}_k^C$ is also anisotropic, with larger energy dissipation at higher horizontal wavenumber κ_r, corresponding to the thin shear layers in the wakes and beside the particle clusters. This is consistent with the anisotropic distribution of $\mathcal{E}_k^C$ presented in figure 13, considering the relationship $\mathcal{D}_k^C = -2\nu\kappa^2\mathcal{E}_k^C$.

4.2.2. *Kinetic energies of the horizontal and vertical velocity components*

As discussed in § 4.1, the particle-induced turbulence is anisotropic with stronger velocity fluctuations in the vertical direction. Therefore, in this subsubsection, we separately investigate the budgets of the fluctuation intensity for the vertical and horizontal components. To this end, we decompose the TKE k into the vertical component $k_v = \langle v^2\rangle/2$ and the horizontal component $k_h = \langle u^2 + w^2\rangle/2$, i.e. $k = k_v + k_h$. Accordingly, the budgets of these vertical energy k_v and horizontal energy k_h are defined by $\mathcal{J}_v = \mathcal{J}_2$ and $\mathcal{J}_h = \mathcal{J}_1 + \mathcal{J}_3$, where $\mathcal{J}$ represents the arbitrary term $\mathcal{T}$, $\mathcal{P}$, $\mathcal{D}$ or $\mathcal{F}$.

First, we illustrate the budget of the vertical component of the kinetic energy in figure 17(*a–c*). By comparing with figure 12, we find that the different contributions to the vertical turbulence kinetic energy are similar to those of the TKE (except for the non-zero pressure term $\mathcal{P}_v$). This observation is explained by the predominance of the vertical fluid

https://doi.org/10.1017/jfm.2025.398 Published online by Cambridge University Press

velocity in the pseudo-turbulent flow induced by the settling particles. It is also shown in figure 17(*a–c*) that the IB forces do positive work in the vertical direction as the source of the vertical kinetic energy. However, examining the budget for the horizontal component shown in figure 17(*d–f*), it is interesting to note that the pressure term $\mathcal{P}_h$ becomes positive and serves as the source of the horizontal kinetic energy. In contrast, the IB forces, which only transfer energy among different scales, have zero net contribution to the horizontal kinetic energy, namely $\sum_{\boldsymbol{\kappa}} \mathcal{F}_h(\boldsymbol{\kappa}) = 0$, similar to the turbulence modulation by finite-sized particles (Chiarini & Rosti 2024). In other words, due to the flow incompressibility, the pressure effectively redistributes part of the energy from the vertical component (as confirmed by the negative value of $\mathcal{P}_v$ in figure 17*a–c*), and thus sustains the horizontal flow energy in this system. It is also noteworthy from figure 17(*d,f*) that the contribution from $\mathcal{P}_h$ is substantially augmented in the FM cases of oblate/prolate particles at large scales. Recalling the significant particle clustering in these cases, we speculate that the enhanced energy redistribution is related to the flow characteristics in the clustering regions. Finally, as a consequence of this redistribution by pressure forces, the unevenly allocated velocity fluctuations of the particle-induced pseudo-turbulence (the anisotropy feature; see table 2) is attenuated when the particle clustering is significant.

Finally, we wish to summarize the whole path of the energy transfer in the pseudo-turbulence induced by settling particles. Because of the settling motion of particles, fluid–particle interaction forces do positive work along the vertical direction, which is the source of energy in the whole flow system. A part of input energy is redistributed from the vertical velocity component to the horizontal components under the action of pressure, which sustains the horizontal velocity fluctuations. The energy is injected into the fluid flow by the settling motion of particles typically on scales larger than the particle size, and then is transferred among different scales by both nonlinear effects and the IB forces. At scales smaller than the particle size, however, viscous dissipation locally balances the work done by fluid–particle interaction forces, leading to the κ^{-3} power law of the energy spectra. The influence of particle clustering on the particle-induced turbulent flows is twofold. On the one hand, column-like particle clusters inject energy at larger scales, giving rise to the emergence of large-scale flow structures. On the other hand, the particle clustering also enhances the energy redistribution by pressure between the vertical and horizontal velocity components, by which the anisotropy of the particle-induced turbulence is attenuated.

5. Conclusions

In the present work, we studied the settling of spheroidal particles with different shape in an initially quiescent fluid by means of PR-DNS. We considered spheroids with aspect ratio $\lambda = 0.5$ (oblate spheroids), $\lambda = 1$ (spheres) and $\lambda = 2$ (prolate spheroids). Under the current parameter set-ups, the isolate spheroid settles vertically without the wake and path instability. However, in the suspension, the dynamics of the settling particles and the fluid flow induced by the particle motion are significantly altered by complicated fluid–particle hydrodynamic interactions. To disentangle these, we performed simulations of freely moving (FM) particles and of an ideal suspension in which the particle relative position is fixed and the orientation is random.

We first examined the collective behaviour of the dispersed phase. It was found that the mean settling velocity is enhanced for oblate/prolate spheroids in the dilute suspension with solid volume fraction $\phi = 1\,\%$. On the one hand, the change of particle orientation, which is caused by the complicated particle–fluid and particle–particle interactions in the suspension, makes a contribution to accelerating the settling motion of spheroidal

https://doi.org/10.1017/jfm.2025.398 Published online by Cambridge University Press

particles, deviating their orientation from the stable broad-side-on alignment. On the other hand, the spheroidal particles were found to form column-like clusters under the effect of the wake-induced hydrodynamic interactions. The settling motion of clustered particles can be enhanced substantially due to the preferential sampling of downward flow, which was confirmed by the correlation between the Voronoi volume (or the cluster size) and the settling velocity of non-spherical particles. Under this effect, the mean settling velocity is enhanced to the maximum degree for the FM oblate particles owing to the most significant particle clustering in that case. By contrast, the mean settling velocity is slightly reduced for spherical particles due to the hindrance effect, since the clustering is not present, and the effect of orientation is irrelevant to settling spheres.

Then we carefully investigated the fluid flow induced by settling particles. Although the wake of an isolated settling particle is steady, the instability induced by wake–wake interactions causes a spatiotemporal evolving flow, i.e. so-called particle-induced pseudo-turbulence. The one-point statistics of the fluid velocity indicate that the pseudo-turbulence is anisotropic, with higher fluctuations of the vertical than horizontal velocity, and the p.d.f.s of the fluid velocity fluctuations are non-Gaussian, similar to the observations in the bubble-induced pseudo-turbulence (Riboux *et al.* 2010; Amoura *et al.* 2017). Moreover, we also identified a robust κ^{-3} power law of the energy spectra in the particle-induced turbulence at scales close to and smaller than the particle size. By further performing the scale-by-scale analysis of the energy budget, this power law of the energy spectra is explained by the local balance between the energy production from the fluid–particle interactions and dissipation (Lance & Bataille 1991).

In addition, we study the directional information of the energy spectra and budget in spectral space. We demonstrate that the anisotropy of the particle-induced turbulent flow is not only manifested by the unequal distribution of the turbulence kinetic energy in the horizontal and vertical velocity components, but also reflected by the anisotropic energy spectra and corresponding budgets in spectral space. The energy spectra are found to decay more rapidly along the vertical direction than the horizontal ones in cylindrical coordinates in spectral space, indicating the smaller scale of the typical horizontal flow structures (i.e. thin shear layers) compared with the longer vertical structures (i.e. wakes or flow streaks). Interestingly, this kind of anisotropic cascade of the energy spectra is less pronounced for the cases with significant particle clustering (i.e. FM oblate or prolate particles), although energy production by the fluid–particle interactions exhibits a higher degree of anistropy in these cases. This is linked to the intensified inter-scale energy transfer by the nonlinear effect when particle clustering is present, which is presumably related to meandering of regions depleted of particles and to the wake–wake interactions. Note that the return to isotropy has been correlated to the local shear in the wakes of rising bubbles (Zamansky *et al.* 2024). Our results seem to confirm that the higher mean shear induced by particle columns indeed facilitates the recovery of isotropy of the fluid flow.

By separately examining the energy budget of the horizontal and vertical velocity components, we disclosed the path of energy transfer in the present flow system. The fluid–particle interactions do work along the vertical direction, which serves as the source of the kinetic energy in this system. Then pressure plays an essential role in redistributing energy among different velocity components, supplying the energy to the horizontal fluid flows. Meanwhile, energy is transferred among different scales by nonlinear effects, and is eventually dissipated by viscosity. Notably, the presence of particle clustering can significantly alter the energy transfer in two ways. On the one hand, column-like particle clusters increase the energy input at the largest scale, giving rise to large-scale flow structures and intensifying the fluid velocity fluctuations. On the other hand, the energy

https://doi.org/10.1017/jfm.2025.398 Published online by Cambridge University Press

redistribution by pressure is also enhanced at large scales, which reduces the anisotropy of the pseudo-turbulence of FM spheroidal particles.

Finally, let us discuss potential extensions of the present study. For one thing, we consider only the scenario where the wake of the single settling particle is steady ($Ga = 80$). It therefore remains to be investigated how the presence of wake and path instabilities at increasing Galileo number influences the features of the particle-induced pseudo-turbulence. For another, it is of interest to further investigate the settling of non-spherical particles in an initially turbulent fluid flow. The interaction between particle-induced pseudo-turbulence and the classic Kolmogorov turbulence is not well understood but is relevant in realistic applications.

Funding. This work is supported by the Natural Science Foundation of China (grant nos 12388101, 92252104, 922522204 and 12472224).

Declaration of interests. The authors report no conflict of interest.

References

AMOURA, Z., BESNACI, C., RISSO, F. & ROIG, V. 2017 Velocity fluctuations generated by the flow through a random array of spheres: a model of bubble-induced agitation. *J. Fluid Mech.* **823**, 592–616.

ANOUKOU, K., BRENNER, R., HONG, F., PELLERIN, M. & DANAS, K. 2018 Random distribution of polydisperse ellipsoidal inclusions and homogenization estimates for porous elastic materials. *Comput. Struct.* **210**, 87–101.

ARDEKANI, M.N., COSTA, P., BREUGEM, W.P. & BRANDT, L. 2016 Numerical study of the sedimentation of spheroidal particles. *Intl J. Multiphase Flow* **87**, 16–34.

BATCHELOR, G.K. 1972 Sedimentation in a dilute dispersion of spheres. *J. Fluid Mech.* **52** (2), 245–268.

BRANDT, L. & COLETTI, F. 2022 Particle-laden turbulence: progress and perspectives. *Annu. Rev. Fluid Mech.* **54** (1), 159–189.

BREUGEM, W.-P. 2012 A second-order accurate immersed boundary method for fully resolved simulations of particle-laden flows. *J. Comput. Phys.* **231** (13), 4469–4498.

CAFLISCH, R.E. & LUKE, J.H.C. 1985 Variance in the sedimentation speed of a suspension. *Phys. Fluids.* **28** (3), 759–760.

CAPECELATRO, J., DESJARDINS, O. & FOX, R.O. 2014 Numerical study of collisional particle dynamics in cluster-induced turbulence. *J. Fluid Mech.* **747**, R2.

CAPECELATRO, J., DESJARDINS, O. & FOX, R.O. 2015 On fluid–particle dynamics in fully developed cluster-induced turbulence. *J.Fluid Mech.* **780**, 578–635.

CHIARINI, A. & ROSTI, M.E. 2024 Finite-size inertial spherical particles in turbulence. *J. Fluid Mech.* **988**, A17.

CHOUIPPE, A. & UHLMANN, M. 2015 Forcing homogeneous turbulence in direct numerical simulation of particulate flow with interface resolution and gravity. *Phys. Fluids.* **27** (12), 123301.

COSTA, P., BOERSMA, B.J., WESTERWEEL, J. & BREUGEM, W.-P. 2015 Collision model for fully resolved simulations of flows laden with finite-size particles. *Phys. Rev. E* **92** (5), 053012.

CRIALESI-ESPOSITO, M., ROSTI, M.E., CHIBBARO, S. & BRANDT, L. 2022 Modulation of homogeneous and isotropic turbulence in emulsions. *J. Fluid Mech.* **940**, A19.

DABADE, V., MARATH, N.K. & SUBRAMANIAN, G. 2015 Effects of inertia and viscoelasticity on sedimenting anisotropic particles. *J. Fluid Mech.* **778**, 133–188.

DI FELICE, R. 1999 The sedimentation velocity of dilute suspensions of nearly monosized spheres. *Intl J. Multiphase Flow* **25** (4), 559–574.

DODDS, D., SARHAN, A.R. & NASER, J. 2020 Experimental and numerical study of drag forces on particles in clusters. *Powder Technol.* **371**, 195–208.

ERN, P., RISSO, F., FABRE, D. & MAGNAUDET, J. 2012 Wake-induced oscillatory paths of bodies freely rising or falling in fluids. *Annu. Rev. Fluid Mech.* **44** (1), 97–121.

FERENC, J.-S. & NÉDA, Z. 2007 On the size distribution of Poisson Voronoï cells. *Physica A: Stat. Mech. Applics.* **385** (2), 518–526.

FORNARI, W., ARDEKANI, M.N. & BRANDT, L. 2018 Clustering and increased settling speed of oblate particles at finite Reynolds number. *J. Fluid Mech.* **848**, 696–721.

FORNARI, W., PICANO, F. & BRANDT, L. 2016 Sedimentation of finite-size spheres in quiescent and turbulent environments. *J. Fluid Mech.* **788**, 640–669.

https://doi.org/10.1017/jfm.2025.398 Published online by Cambridge University Press

FORNARI, W., ZADE, S., BRANDT, L. & PICANO, F. 2019 Settling of finite-size particles in turbulence at different volume fractions. *Acta Mechanica* **230** (2), 413–430.
FORTES, A.F., JOSEPH, D.D. & LUNDGREN, T.S. 1987 Nonlinear mechanics of fluidization of beds of spherical particles. *J. Fluid Mech.* **177**, 467–483.
FRÖHLICH, K., MEINKE, M. & SCHRÖDER, W. 2020 Correlations for inclined prolates based on highly resolved simulations. *J. Fluid Mech.* **901**, A5.
GARSIDE, J. & AL-DIBOUNI, M.R. 1977 Velocity-voidage relationships for fluidization and sedimentation in solid–liquid systems. *Ind. Engng Chem. Process Des. Dev.* **16** (2), 206–214.
GUALTIERI, P., BATTISTA, F. & CASCIOLA, C.M. 2017 Turbulence modulation in heavy-loaded suspensions of tiny particles. *Phys. Rev. Fluids* **2** (3), 034304.
GUALTIERI, P., PICANO, F., SARDINA, G. & CASCIOLA, C.M. 2013 Clustering and turbulence modulation in particle-laden shear flows. *J. Fluid Mech.* **715**, 134–162.
GUAZZELLI, É. & HINCH, J. 2011 Fluctuations and instability in sedimentation. *Annu. Rev. Fluid Mech.* **43** (1), 97–116.
HIDMAN, N., STRÖM, H., SASIC, S. & SARDINA, G. 2023 Assessing passive scalar dynamics in bubble-induced turbulence using direct numerical simulations. *J. Fluid Mech.* **962**, A32.
HÖFLER, K. & SCHWARZER, S. 2000 Navier–Stokes simulation with constraint forces: finite-difference method for particle-laden flows and complex geometries. *Phys. Rev. E* **61** (6), 7146–7160.
HUISMAN, S.G., BAROIS, T., BOURGOIN, M., CHOUIPPE, A., DOYCHEV, T., HUCK, P., MORALES, C.E.B., UHLMANN, M. & VOLK, R. 2016 Columnar structure formation of a dilute suspension of settling spherical particles in a quiescent fluid. *Phys. Rev. Fluids* **1** (7), 074204.
INNOCENTI, A., JACCOD, A., POPINET, S. & CHIBBARO, S. 2021 Direct numerical simulation of bubble-induced turbulence. *J. Fluid Mech.* **918**, A23.
JEFFREY, D.J. 1982 Low-Reynolds-number flow between converging spheres. *Mathematika* **29** (1), 58–66.
JENNY, M., DUEK, J. & BOUCHET, G. 2004 Instabilities and transition of a sphere falling or ascending freely in a Newtonian fluid. *J. Fluid Mech.* **508**, 201–239.
JIANG, X., HUANG, W., XU, C. & ZHAO, L. 2024*a* A flow-reconstruction based approach for the computation of hydrodynamic stresses on immersed body surface. *J. Comput. Phys.* **508**, 113025.
JIANG, X., XU, C. & ZHAO, L. 2024*b* Prolate spheroids settling in a quiescent fluid: clustering, microstructures and collisions. *J. Fluid Mech.* **1000**, A49.
JIANG, X., XU, C. & ZHAO, L. 2024*c* Settling and collision of spheroidal particles with an offset mass centre in a quiescent fluid. *J. Fluid Mech.* **984**, A40.
KAJISHIMA, T. 2004 Influence of particle rotation on the interaction between particle clusters and particle-induced turbulence. *Intl J. Heat Fluid Flow* **25** (5), 721–728.
KAJISHIMA, T. & TAKIGUCHI, S. 2002 Interaction between particle clusters and particle-induced turbulence. *Intl J. Heat Fluid Flow* **23** (5), 639–646.
KIM, K., BAEK, S.-J. & SUNG, H.J. 2002 An implicit velocity decoupling procedure for the incompressible Navier–Stokes equations. *Intl J. Numer. Meth. Fluids* **38** (2), 125–138.
KOCH, D.L. & HILL, R.J. 2001 Inertial effects in suspension and porous-media flows. *Annu. Rev. Fluid Mech.* **33** (1), 619–647.
LANCE, M. & BATAILLE, J. 1991 Turbulence in the liquid phase of a uniform bubbly air–water flow. *J. Fluid Mech.* **222**, 95–118.
LE ROY DE BONNEVILLE, F., ZAMANSKY, R., RISSO, F., BOULIN, A. & HAQUET, J.-F. 2021 Numerical simulations of the agitation generated by coarse-grained bubbles moving at large Reynolds number. *J. Fluid Mech.* **926**, A20.
LUCCI, F., FERRANTE, A. & ELGHOBASHI, S. 2010 Modulation of isotropic turbulence by particles of Taylor length-scale size. *J. Fluid Mech.* **650**, 5–55.
MARTÍNEZ-MERCADO, J., PALACIOS-MORALES, C.A. & ZENIT, R. 2007 Measurement of pseudoturbulence intensity in monodispersed bubbly liquids for $10 < Re < 500$. *Phys. Fluids.* **19** (10), 103302.
MEHRABADI, M., TENNETI, S., GARG, R. & SUBRAMANIAM, S. 2015 Pseudo-turbulent gas-phase velocity fluctuations in homogeneous gas–solid flow: fixed particle assemblies and freely evolving suspensions. *J. Fluid Mech.* **770**, 210–246.
MONCHAUX, R., BOURGOIN, M. & CARTELLIER, A. 2010 Preferential concentration of heavy particles: a Voronoï analysis. *Phys. Fluids.* **22** (10), 103304.
MORICHE, M., HETTMANN, D., GARCÍA-VILLALBA, M. & UHLMANN, M. 2023 On the clustering of low-aspect-ratio oblate spheroids settling in ambient fluid. *J. Fluid Mech.* **963**, A1.
PANDEY, V., MITRA, D. & PERLEKAR, P. 2023 Kolmogorov turbulence coexists with pseudo-turbulence in buoyancy-driven bubbly flows. *Phys. Rev. Lett.* **131** (11), 114002.

https://doi.org/10.1017/jfm.2025.398 Published online by Cambridge University Press

PANDEY, V., RAMADUGU, R. & PERLEKAR, P. 2020 Liquid velocity fluctuations and energy spectra in three-dimensional buoyancy-driven bubbly flows. *J. Fluid Mech.* **884**, R6.

PRUPPACHER, H.R. & KLETT, J.D. 2010 *Microphysics of Clouds and Precipitation*. Springer.

RAMIREZ, G., BURLOT, A., ZAMANSKY, R., BOIS, G. & RISSO, F. 2024 Spectral analysis of dispersed multiphase flows in the presence of fluid interfaces. *Intl J. Multiphase Flow* **177**, 104860.

RIBOUX, G., RISSO, F. & LEGENDRE, D. 2010 Experimental characterization of the agitation generated by bubbles rising at high Reynolds number. *J. Fluid Mech.* **643**, 509–539.

RICHARDSON, J.F. & ZAKI, W.N. 1954 The sedimentation of a suspension of uniform spheres under conditions of viscous flow. *Chem. Engng Sci.* **3** (2), 65–73.

RISSO, F. 2011 Theoretical model for k^{-3} spectra in dispersed multiphase flows. *Phys. Fluids.* **23** (1), 011701.

RISSO, F. 2018 Agitation, mixing, and transfers induced by bubbles. *Annu. Rev. Fluid Mech.* **50** (1), 25–48.

ROGHAIR, I., MERCADO, J.M., VAN SINT ANNALAND, M., KUIPERS, H., SUN, C. & LOHSE, D. 2011 Energy spectra and bubble velocity distributions in pseudo-turbulence: numerical simulations vs. experiments. *Intl J. Multiphase Flow* **37** (9), 1093–1098.

ROMA, A.M., PESKIN, C.S. & BERGER, M.J. 1999 An adaptive version of the immersed boundary method. *J. Comput. Phys.* **153** (2), 509–534.

ROSSI, E., BAGHERI, G., BECKETT, F. & BONADONNA, C. 2021 The fate of volcanic ash: premature or delayed sedimentation? *Nat. Commun.* **12** (1), 1303.

SEYED-AHMADI, A. & WACHS, A. 2021 Sedimentation of inertial monodisperse suspensions of cubes and spheres. *Phys. Rev. Fluids* **6** (4), 044306.

SHAJAHAN, T. & BREUGEM, W.-P. 2023 Inertial effects in sedimenting suspensions of solid spheres in a liquid. *Intl J. Multiphase Flow* **166**, 104498.

TAGAWA, Y., ROGHAIR, I., PRAKASH, V.N., VAN SINT ANNALAND, M., KUIPERS, H., SUN, C. & LOHSE, D. 2013 The clustering morphology of freely rising deformable bubbles. *J. Fluid Mech.* **721**, R2.

TRUDNOWSKA, E., LACOUR, L., ARDYNA, M., ROGGE, A., IRISSON, J.O., WAITE, A.M., BABIN, M. & STEMMANN, L. 2021 Marine snow morphology illuminates the evolution of phytoplankton blooms and determines their subsequent vertical export. *Nat. Commun.* **12** (1), 2816.

UHLMANN, M. 2005 An immersed boundary method with direct forcing for the simulation of particulate flows. *J. Comput. Phys.* **209** (2), 448–476.

UHLMANN, M. 2020 Voronoï tessellation analysis of sets of randomly placed finite-size spheres. *Physica A* **555**, 124618.

UHLMANN, M. & DOYCHEV, T. 2014 Sedimentation of a dilute suspension of rigid spheres at intermediate Galileo numbers: the effect of clustering upon the particle motion. *J. Fluid Mech.* **752**, 310–348.

VOTH, G.A. & SOLDATI, A. 2017 Anisotropic particles in turbulence. *Annu. Rev. Fluid Mech.* **49** (1), 249–276.

WANG, L.-P., AYALA, O., GAO, H., ANDERSEN, C. & MATHEWS, K.L. 2014 Study of forced turbulence and its modulation by finite-size solid particles using the lattice Boltzmann approach. *Comput. Maths Applics.* **67** (2), 363–380.

YIN, X. & KOCH, D.L. 2007 Hindered settling velocity and microstructure in suspensions of solid spheres with moderate Reynolds numbers. *Phys. Fluids.* **19** (9), 093302.

ZAIDI, A.A. 2018 Particle velocity distributions and velocity fluctuations of non-Brownian settling particles by particle-resolved direct numerical simulation. *Phys. Rev. E* **98** (5), 053103.

ZAIDI, A.A. 2021 Domain size effects on particle microstructures settling in non-Stokes regime. In *International Bhurban Conference on Applied Sciences and Technologies (IBCAST)*, pp. 748–753.

ZAIDI, A.A., TSUJI, T. & TANAKA, T. 2014 Direct numerical simulation of finite sized particles settling for high Reynolds number and dilute suspension. *Intl J. Heat Fluid Flow* **50**, 330–341.

ZAMANSKY, R., LE ROY DE BONNEVILLE, F. & RISSO, F. 2024 Turbulence induced by a swarm of rising bubbles from coarse-grained simulations. *J. Fluid Mech.* **984**, A68.

ZASTAWNY, M., MALLOUPPAS, G., ZHAO, F. & VAN WACHEM, B. 2012 Derivation of drag and lift force and torque coefficients for non-spherical particles in flows. *Intl J. Multiphase Flow* **39**, 227–239.

ZHOU, Z.Y., PINSON, D., ZOU, R.P. & YU, A.B. 2011 Discrete particle simulation of gas fluidization of ellipsoidal particles. *Chem. Engng Sci.* **66** (23), 6128–6145.

https://doi.org/10.1017/jfm.2025.398 Published online by Cambridge University Press